

## Terahertz oscillation of 180° domain walls in ferroelectric membranes

Xiangwei Guo<sup>1a</sup>), Jiakuan Wu<sup>1a</sup>), Yujie Zhu<sup>1</sup>, Aiden Ross<sup>2</sup>, Bo Wang<sup>2</sup>, Paul G. Evans<sup>1</sup>, Long-Qing Chen<sup>2</sup>, and Jia-Mian Hu<sup>1\*</sup>

<sup>1</sup>*Department of Materials Science and Engineering, University of Wisconsin-Madison, Madison, WI, 53706, USA*

<sup>2</sup>*Department of Materials Science and Engineering, The Pennsylvania State University, University Park, Pennsylvania, 16802, USA*

### Abstract

A fundamentally intriguing yet not well understood topic in the field of ferroelectrics is the collective excitation of domain walls (DWs), with potential applications to DW-based nanoelectronic and optoelectronic devices. Here we use dynamical phase-field simulations to identify the collective modes of an Ising-type 180° DW in a uniaxially strained BaTiO<sub>3</sub> membrane. The membrane concurrently functions as a cavity for polarization and acoustic waves and permits cavity-enhanced resonant excitation of polarization waves. The simulation reveals an unconventional DW sliding mode that exhibits a depolarization-field-driven nonzero resonant frequency and a dynamically changing internal structure during sliding. These features differ from the previously reported DW sliding modes that have a zero resonant frequency or a rigid internal structure. An analytical model is developed to quantitatively understand the origin of this new DW mode and predict the effect of strain on the mode frequency. The analytically predicted strain dependence of the frequencies of the unconventional DW sliding mode and the DW breathing mode, both in the terahertz regime, is further validated by dynamical phase-field simulations. These results provide new insights into the high-frequency dynamics of ferroelectric DWs and suggest opportunities for realizing on-demand control of phonon-DW resonance by strain, and more broadly, discovering and controlling unconventional DW modes in conventional domain patterns, with applications to reconfigurable THz and optical devices.

\*E-mail: [jhu238@wisc.edu](mailto:jhu238@wisc.edu)

<sup>a</sup>)X. Guo and J. Wu contribute equally to this work.

## 1. Introduction

Ferroic membranes can be integrated with materials with different crystal structure and composition through lift-off and transferring [1-6], and can enable large, continuously tunable strain, strain gradient and more complex deformation modes [7] (e.g., stretching [8-10], bending [11,12], rippling [13,14], folding [15], and twisting [16]) that are difficult to achieve in films grown on an elastically stiff substrate [17]. Capitalizing on these capabilities, ferroic membranes have thus far been exploited for stabilizing topologically nontrivial structures [5,16,18] and realizing extreme-state strain engineering of materials properties [15,19-21], with potential applications to flexible electronic, spintronic, and micro-electromechanical devices [22-27]. The high-frequency dynamics of these membranes may exhibit novel time-dependent phenomena not available in supported ferroic thin films but are comparatively unexplored. Here we computationally show that ferroelectric membranes can concurrently function as a cavity for both the coherent polarization waves and acoustic waves, enabling cavity-enhanced resonant excitation of polarization waves. Using a uniaxially strained BaTiO<sub>3</sub> membrane with archetypical Ising-type 180° domain walls (DWs) as an example, we discover an unconventional terahertz DW sliding mode with a strain-tunable mode frequency by dynamical phase-field modeling (DPFM).

DPFM has been extensively used to predict the responses of polarization (especially the topological polar textures [28-32]) to external stimuli in ferroelectric bulk crystals [33-35] and thin films [36] as well as in strained ferroelectric/dielectric superlattice thin films [28-30,32,37]. Recently, by incorporating the coupled dynamics of polarization, strain, and electromagnetic (EM) waves [38], DPFM has been extended to enable the study of EM wave transmission through the ferroelectric material [39-41]. Molecular dynamics simulations have also been used to predict the formation and switching dynamics of ferroelectric domains in bulk crystals [42-45], strained thin films [46-50] and ferroelectric/dielectric superlattice thin films [51,52]. Experimentally, new collective modes have recently been discovered [28,31,37] through the excitation of topological polar textures (vortices and skyrmions) in PbTiO<sub>3</sub>/SrTiO<sub>3</sub> superlattice thin films by a terahertz (THz) electric-field pulse. However, there have been few studies of the coupled dynamics of polarization waves and acoustic waves in multidomain ferroelectric membranes.

Here, we hypothesize that ferroelectric membranes permit the excitation of large-amplitude, THz DW oscillation via cavity-enhanced resonant interaction between the acoustic waves and the DW modes. We further hypothesize that strain can effectively tune the frequencies of the DW modes, thereby achieving an on-demand activation of phonon-DW resonance. These hypotheses are demonstrated using a uniaxially strained BTO membranes containing Ising-type 180° DWs as an example. We employ the dynamical phase-field simulation of the dynamics of ferroelectric domain formation to obtain the frequency-wavevector dispersion relation of the polarization waves. The modes of polarization waves include both the intrinsic modes, i.e., those that would appear in a single-domain ferroelectric, and the DW modes. Guided by the dispersion relation, we find strategies for the selective excitation of individual modes by a THz pulse and reconstruct the mode profiles. Based on the simulation results and complementary analytical modeling, we demonstrate the selective excitation of a DW breathing mode predicted recently by an analytical calculation [53], and notably, an unconventional DW sliding mode, both of which are at a terahertz (THz)-regime resonant frequency. The frequencies of these modes can be effectively tuned by strain, as predicted by both an analytical model and dynamical phase-field simulations. Our results provide new insights into the collective excitation of ferroelectric DWs and suggest potential applications of domain-engineered ferroelectric nanomembranes in wave-based computing [54] and THz wave generation [55].

## 2. Intrinsic modes of coherent polarization waves

We first study the intrinsic modes of coherent polarization waves. A single-domain, uniaxially strained BTO membrane with a spontaneous polarization along  $+x_1$  is shown in Fig. 1(a). The single-domain state is obtained by performing 3D dynamical phase-field simulations under a constant temperature of 300 K and constant total strain  $\varepsilon_{11}$  of 0.7%, where the local polarization vectors in the initial state ( $t=0$ ) all align along  $+x_1$  but have a small magnitude fluctuating near  $0.01 \text{ C/m}^2$ . This initial state mimics the paraelectric state. The membrane undergoes an isothermal paraelectric-to-ferroelectric phase transition, forming a single domain at equilibrium. Specifically, all the local polarization evolves from a near-zero but positive value to its nearest energy minimum at  $P_1^{\text{eq}}=0.26 \text{ C/m}^2$ , as shown in Fig. 1(b). Details of the dynamical phase-field simulations are in Appendix A. Figure 1(c) shows the polarization oscillation in the center of the membrane,  $\Delta P_1(t)=P_1-P_1(t=0)$ . The corresponding frequency spectrum is shown in Fig. 1(d).

In the initial stage of domain formation, the initial small-amplitude polarization vectors rapidly grow towards  $P_1^{\text{eq}}$ , manifesting as the growth of polarization wave [56], which is analogous to the growth of concentration wave in spinodal decomposition. Figure 1(e) shows the profiles of transverse polarization wave  $\Delta P_1(x_2, t)$  along the dashed line indicated in Fig. 1(a) at several representative moments of the initial growth stage. Averaging such line profile along the  $x_1$  axis within the  $x_1$ - $x_2$  plane and then performing 2D Fourier transform of the averaged  $\langle \Delta P_1 \rangle(x_2, t)$ , gives the dispersion relation, represented by  $\langle \Delta P_1 \rangle(k_2, f)$ , in Fig. 1(f). Here  $k_2$  and  $f$  are the angular wavenumber and temporal frequency, respectively. In Fig. 1(f), the temporal axis of the Fourier transform considered the time period from  $t=10$  to 200 ps. The polarization evolution in this time period exhibits the oscillations around  $P_1^{\text{eq}}$  that are apparent in Fig. 1(b) and is thus the most insightful range for the dispersion relation analysis.

We made three main observations from Fig. 1(f). First, there is a frequency band from 4-6 THz that has a parabolic dependence on the wavevector. The frequencies in this range are consistent with the single-point frequency spectrum in Fig. 1(d). The lower-bound trajectory of the frequency band in Fig. 1(f) agrees well with the analytically calculated dispersion relation of the soft mode. In the tetragonal BTO, the soft mode is the A1 transverse optical phonon [57], which has the form  $\omega_f^2 = \omega_0^2 + (G_0/\mu)k_2^2$ , where  $\omega_0/2\pi=4.14 \text{ THz}$  is the temporal frequency of the soft-mode phonon at  $k_2=0$ ,  $G_0$  is the isotropic gradient energy coefficient, and  $\mu$  is the isotropic mass coefficient for polarization dynamics. Details of analytical calculation are shown in Appendix B. Modes that have higher frequency than  $\omega_0/2\pi$  in the 4-6 THz band are caused by the unavoidable numerical issue of applying Fourier transform to a discrete system, which sets the upper-bound of the wavenumber approximately be the inverse of the simulation grid size. Doubling the grid size does not alter  $\omega_f$  yet results in a halved frequency band. Second, there exist polarization wave modes with frequencies 1 THz that overlap significantly with the analytically calculated transverse acoustic (TA) phonons. These lower-frequency modes have large spectral amplitudes because their  $\omega$  and  $k_2$  match those of TA phonons. We therefore call these lower-frequency polarization waves *acoustic* modes. Acoustic modes are expected only in the stage of the growth of polarization wave [Fig. 1(e)]. We further perform 2D Fourier transform of the averaged  $\langle \Delta P_1 \rangle(x_2, t)$  for  $t=100$ -200 ps. As shown in Fig. 1(g), only the dispersion of soft mode can be observed. Third, all polarization wave modes, including both the soft mode and the acoustic mode, have discrete wavenumbers with  $k_2/2\pi=n/(2L)$  for integer  $n=1, 2, \dots$ , due to the finite size of the membrane ( $L$ ) along the  $x_2$  axis.

### 3. Coherent polarization waves confined to domain walls

We now turn to studying the DW modes by extracting the dispersion relation of coherent polarization waves in stripe domains. The striped domains containing Ising-type  $180^\circ$  DWs is obtained by setting  $P_i(\mathbf{r}, t=0)$  to be along the  $+x_1$  or  $-x_1$  axis, with  $P_1 \approx \pm 0.01$  C/m<sup>2</sup> and  $P_2=P_3=0$ , in eight prescribed regions and letting the system evolve to equilibrium. The simulations employed a constant temperature of 300 K and a constant  $\varepsilon_{11}$  of 0.7%. The polarization charges are screened by mobile charges at all four free surfaces ( $x_1$ - $x_3$  and  $x_1$ - $x_2$  surfaces). Figure 2(a) shows the equilibrium multidomain structure and the corresponding line profile of the polarization is shown in Fig. 2(b). The polarization evolution at a single point in the domain center is almost the same as in the single-domain case in Fig. 1(c). To identify the DW modes, we plot the polarization evolution at the DW, as shown in Fig. 2(c). Figure 2(d) shows their frequency spectra obtained using Fourier transforms of the time-domain data in Fig. 2(c) for the time period of  $t=10$ -200 ps. Multiple peaks are observed in the range of 0-6 THz, which are associated with both the intrinsic modes and the DW modes. The frequencies of intrinsic modes are generally higher than the DW modes due to the expected larger effective mass of a DW than the effective mass of a soft mode.

To understand the DW modes of an Ising-type  $180^\circ$  wall, we extend the eigenmode analysis that was reported for bulk [53] and strained thin-film [58] ferroelectrics to the present case of a uniaxially strained membrane. Details of the eigenmode analysis are shown in Appendix C. The spatial polarization profiles corresponding to the first two eigenmodes are shown in Figs. 2(e-f), which exhibit, respectively, (i) a DW sliding mode with zero resonant frequency and (ii) a breathing mode which manifests as a periodically increasing and decreasing DW thickness with a temporal resonant frequency of 2.94 THz. The third-order DW eigenmode displays an asymmetric profile and has a high temporal resonant frequency of 3.95 THz. This mode is not plotted here because it has a shorter lifetime and lower amplitude than the first two eigenmodes, and because it is numerically challenging to disentangle it from the 4.14-THz soft mode.

The periodic domains along with the two free surfaces with a normal along  $x_2$  (such free surfaces are uniquely possible in a freestanding membrane) allow for amplifying both the intrinsic and DW modes through cavity-enhanced resonant interaction with band-folded standing acoustic phonons. Figure 2(g) shows the analytically calculated band-folded dispersion relation of TA phonons (see Appendix D for details of calculation). The lifetime of these TA phonons is proportional to  $1/\omega^2$ , which is represented with color in Fig. 2(g). Therefore, the polarization wave modes, if their  $\omega$  and  $k_2$  match those of the band-folded TA phonons, would be resonantly enhanced due to the electromechanical coupling. This is analogous to the resonant interaction between acoustic waves (acoustic phonons) and spin waves (magnons) via the magnetoelastic coupling [59-61]. Moreover, the domain periodicity  $D=16$  nm (i.e., the width of a single domain) leads to a new set of discrete wavenumbers  $k_2/2\pi=n/2D$ . Furthermore, because the DW modes do not propagate, they appear as a non-dispersive band in the simulated dispersion relation, as shown in Fig. 2(h). Similarly to Fig. 1(f), there also exists a parabola-shaped frequency band whose lower-bound trajectory agrees well with the analytically calculated soft-mode dispersion relation.

### 4. Selective excitation, profile reconstruction, and strain-modulation of DW modes

The analytically calculated 2.94-THz DW breathing mode is close to the 2.6 THz peak in Fig. 2(d), where there also exist many other peaks that could result from the nonlinear interaction of different modes and/or the anharmonicity of the free energy landscape. To selectively excite the DW breathing mode, we apply a narrowband THz pulse with a center frequency of 2.5 THz and a full-width-half-maximum bandwidth of 0.18 THz [Figs. 3(a,b)] to the equilibrium stripe domain

shown in Fig. 2(a). Figure 3(c,d) show the polarization oscillation at the single cells in the domain center and domain wall regions, respectively, for  $t=20-60$  ps. Within this time period, the applied electric field has become almost zero, thus the polarization oscillation can better represent the behaviors of both the intrinsic and DW modes. The frequency spectrum in Fig. 3(e), which corresponds to the polarization oscillation in the domain center [Fig. 3(c)], shows two strong peaks at 4.18 GHz and 4.9 GHz. Based on the analytically calculated soft-mode dispersion relation, these two peaks characterize the  $k_2/2\pi \approx 0.06 \text{ nm}^{-1}$  ( $n=1$ ) and  $k_2/2\pi \approx 0.31 \text{ nm}^{-1}$  ( $n=5$ ) soft mode, respectively. The spectrum in Fig. 3(f), which corresponds to the polarization oscillation at the DW [Fig. 3(d)], contains not only the peaks shown in Fig. 3(e), but also the lower-frequency ones including the highest peak near 2.45 THz and the second highest peak near 1.52 THz. These features are consistent with the dispersion relation of the polarization wave shown in Fig. 3(g).

Figure 3(h-i) show the spatiotemporal evolution of the DW polarization profile reconstructed selectively for the 2.45 THz and 1.52 THz peak, respectively, via the inverse Fourier transform. Detailed data processing procedures are provided in Appendix E. The profile in Fig. 3(h) indicates a well-defined DW breathing mode, where the local polarization at the two grids in the DW center shift towards (away from) the horizontal line of  $P_1=0$  during the expansion (reduction) of the DW thickness. This is further confirmed by the 2D polarization distribution reconstructed for the 2.45 THz oscillation (also shown in Appendix E). The 1D profile shown in Fig. 3(i) appears to be a DW sliding mode with the polarization at the DW always move along the same direction, which seems puzzling for two reasons. First, the canonical DW sliding mode has a zero energy (resonant frequency) due to the zero restoring force. Second, unlike the case in [62] where the depolarization field induced by the surface polarization charges provides a restoring force, there are no bound polarization charges at the two  $x_2$ - $x_3$  surfaces herein due to the use of periodic boundary condition.

With these in mind, we reconstruct the 2D spatiotemporal distribution of polarization oscillation at 1.52 THz via the inverse Fourier transform. The results, as shown in Fig. 4(a), reveal the presence of an unconventional DW mode that slides along the  $x_2$  axis but has a wavy, dynamically evolving polarization distribution along the  $x_1$  axis, as opposed to moving as a rigid body with uniform distribution along  $x_1$  (as in the case for the zero-energy DW sliding mode). Therefore, we hypothesize that the depolarization field along the  $x_1$  axis tends to straighten the wavy DW and thereby provides a restoring force for DW sliding along the  $x_2$  axis, as shown schematically in Fig. 4(b). An analytical model is then developed (see Appendix F) to quantitatively understand the role of the depolarization field and predict the effect of strain on the frequency of this unconventional DW sliding mode. As shown by the analytical prediction in Fig. 4(c), varying the uniaxial strain  $\varepsilon_{11}$  from 0.5% to 1.5% at 300 K, where the BTO membrane is in the tetragonal phase with  $180^\circ$  DWs (see temperature-strain stability diagram in Appendix G), modulates the frequency of the wavy DW sliding mode from 1.43 THz to 1.77 THz. This prediction is consistent with the results from additional dynamical phase-field simulations, where the moderate deviation is attributed to the simplified treatment on the depolarization field in the analytical model. This relatively small tuning is reasonable because the restoring force of such unconventional DW sliding mode solely results from the depolarization field, which is only influenced by strain indirectly. In contrast, strain-modulation of the resonant frequencies of soft-mode phonon and DW breathing mode, which is also plotted in Fig. 4(c), both exhibits a much wider frequency tuning range. This is because the restoring forces of both the soft mode and DW breathing mode are directly related to the variation of elastic energy, as shown in Appendix B and C. Furthermore, since the dispersion relation of the band-folded acoustic phonons, Fig. 2(g), is expected to be largely strain-independent, strain tuning of DW mode frequencies enables a strain

control of mode-specific phonon-DW resonance in the THz range. This capability can potentially be utilized to design reconfigurable THz and optical devices.

## 5. Conclusions

In summary, we performed dynamical phase-field simulations of the coupled polarization-strain dynamics during the formation of striped ferroelectric domains with Ising-type  $180^\circ$  domain walls (DWs) in uniaxially strained ferroelectric membranes, using  $\text{BaTiO}_3$  as an example. From the simulation results, we identified allowable modes of coherent polarization waves, including both the soft mode and various DW modes, which can all be resonantly amplified by band-folded acoustic phonons of similar frequencies and wavenumbers. Based on subsequent simulations of mode-specific excitation by a narrowband THz pulse, we numerically reconstructed the spatiotemporal profiles of individual polarization wave modes.

Using guidance from analytical modeling, we unraveled and reconstructed the profiles of a canonical DW breathing mode [53], and notably, an unconventional DW sliding mode which has a non-zero resonant frequency and dynamically changing internal profile. We demonstrated, using both analytical calculation and dynamical phase-field simulations, that the frequencies of both the soft mode and these DW modes can be effectively tuned by strain. Experimentally, we expect that these modes can be excited by a single-cycle broadband THz pulse and probed by X-ray or optical pulses, similarly to the experimental discovery of the collective modes of topological polar textures in strained  $\text{PbTiO}_3/\text{SrTiO}_3$  thin-film superlattices [28,31,37]. Furthermore, although the periodic domain patterns enable a mode-specific control of phonon-DW resonance, the excitation of the DW modes predicted herein does not necessarily require a perfectly periodic domain pattern. Rather, any ferroelectric membranes that have stripe domains with  $180^\circ$  DWs, such as the uniaxially strained  $\text{SrTiO}_3$  membrane [19], can be used to validate the predictions in this work.

Overall, our findings provide new insights into the nature of the collective excitation of ferroelectric DWs via a combined theoretical and computational predicting of cavity-enhanced DW-phonon resonance, strain modulation, and new DW mode. These results suggest that there still exist ample opportunities for discovering unconventional DW modes in ferroelectric materials with conventional domain patterns, such as striped domains with  $90^\circ$  and  $109^\circ$  DWs (see Appendix G for examples). The fundamental understanding established through these relatively simple domain patterns will benefit the search for new collective modes from a wide range of topologically nontrivial polar textures [63-66]. Furthermore, by analogy to the strong magnon-phonon coupling in magnetic multilayers [67-70] and freestanding magnetic membranes [61], it would be possible to create new hybridized states via cavity-enhanced strong coupling between coherent polarization waves and acoustic waves [71], which can potentially be utilized to design new hybrid dynamical and quantum systems [72] for realizing new functionalities in quantum communication, computing, and sensing.

## Acknowledgements

The dynamical phase-field simulations in this work are primarily funded by the National Science Foundation (NSF) under Grant No. DMR-2237884 (X.G. and J.-M.H.) and partially funded by the Wisconsin MRSEC (DMR-2309000) (X.G., J.W., and J.-M.H.). The dynamical phase-field simulations were performed using Bridges at the Pittsburgh Supercomputing Center through allocation TG-DMR180076 from the Advanced Cyberinfrastructure Coordination Ecosystem: Services & Support (ACCESS) program, which is supported by NSF Grants No. 2138259, No. 2138286, No. 2138307, No. 2137603, and No. 2138296. The theoretical works on the analytical

calculation of domain wall modes are funded by the US Department of Energy, Office of Science, Basic Energy Sciences, under Award Number DE-SC0020145 as part of the Computational Materials Sciences Program (Y.Z., L.-Q.C., and J.-M.H.). A.R. acknowledges the support of the National Science Foundation Graduate Research Fellowship Program under Grant No. DGE1255832.

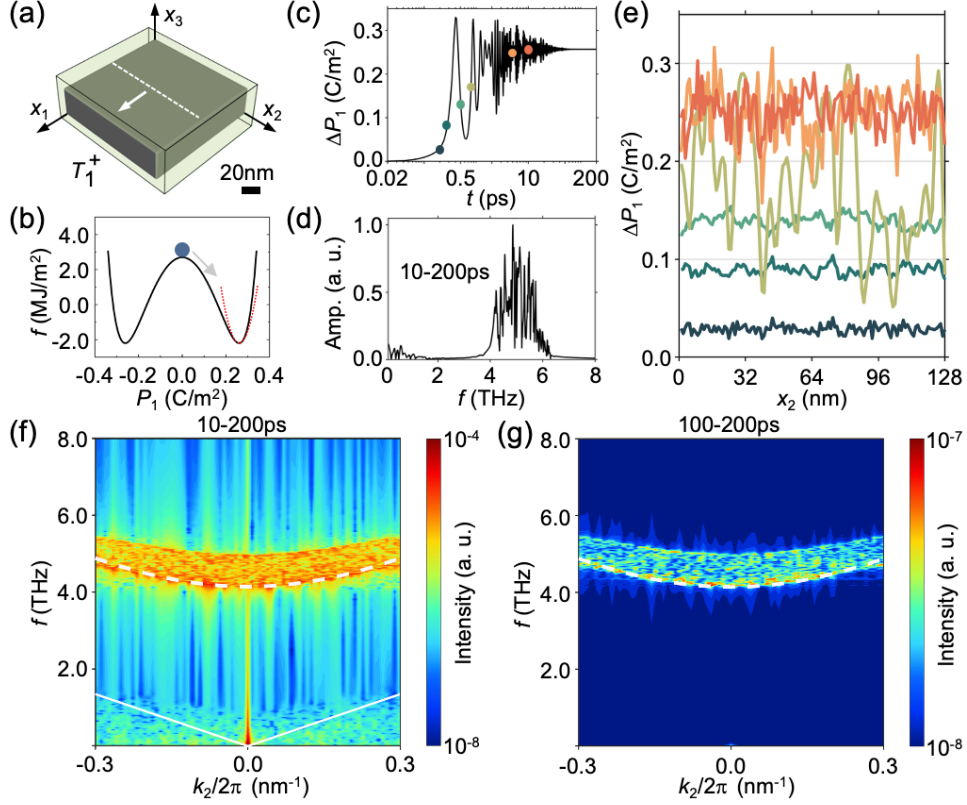


**Fig. 1.** (a) Equilibrium single-domain structure of a 32-nm-thick uniaxial strained BTO membrane with  $\varepsilon_{11}=0.7\%$ , obtained by dynamical phase-field simulations. The arrow indicates the direction of spontaneous polarization. The dashed line cuts through middle plane at  $x_3=16$  nm and  $x_1=64$  nm. The cuboid with black frames represents the entire simulation system with air surrounding the membrane. (b) 1D free energy density of a single-domain BaTiO<sub>3</sub> membrane calculated by fixing the total strain tensor to those at the initial equilibrium condition ( $P_i=P_i^{\text{eq}}$ ) at  $\varepsilon_{11}=0.7\%$  and varying the eigenstrain  $\varepsilon_i^0$  based on the  $P_1$ , with  $P_2=P_3=0$ . The red dashed line indicates the harmonic fitting of the free energy profile, which shows  $|\Delta P_1| \leq 0.001$  C/m<sup>2</sup> within the harmonic regime. (c) Evolution of  $\Delta P_1$  at the center of the simulation system at  $(x_1, x_2, x_3)=(64$  nm, 64 nm, 16 nm).  $t=0$  indicates the initial paraelectric phase. (d) Frequency spectrum calculated by performing Fourier transform of the time-domain data in (c) for  $t=10$ -200 ps. (e) Spatial profiles of the  $\Delta P_1$  along the dashed line in (a) at  $t=0.2$  ps, 0.28 ps, 0.5 ps, 0.8 ps, 6.0 ps and 10.0 ps, corresponding to the dots in (c). Dispersion relation of coherent polarization wave, represented by  $\langle \Delta P_1 \rangle(k_2, f)$ , calculated by performing 2D Fourier transform of the  $\langle \Delta P_1 \rangle(x_2, t)$  for (f)  $t=10$ -200 ps and (g)  $t=100$ -200 ps. In (f), the white dashed curve and solid line indicate the analytically calculated dispersion of the soft mode and the transverse acoustic phonons, respectively.

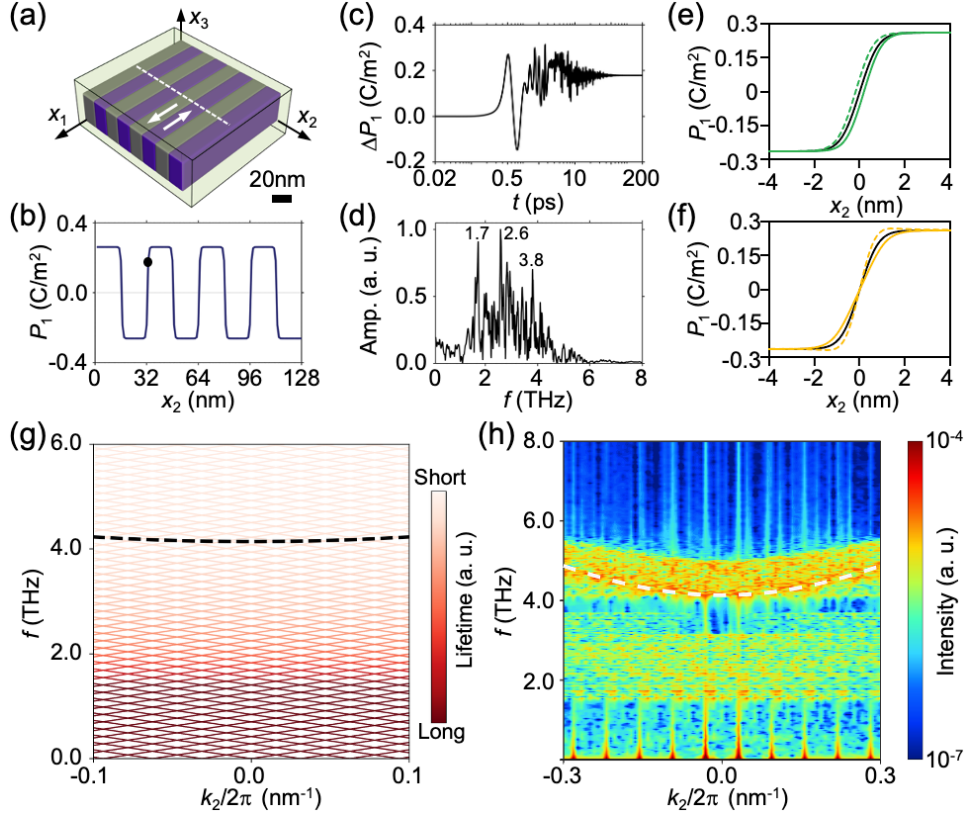


**Fig. 2.** (a) Equilibrium stripe domain structure for a 32-nm-thick uniaxial strained BTO membrane with  $\varepsilon_{11}=0.7\%$ , obtained by dynamical phase-field simulations. The arrows indicate the direction of local spontaneous polarization. The location of the dashed line is the same as that in Fig. 1(a). (b) The spatial profile of polarization  $P_1$  along the dashed line in Fig. 1(a), where  $P_2 \approx 0$ ,  $P_3 \approx 0$ . (c) Evolution of  $\Delta P_1$  at the DW, represented by the point in (b).  $t=0$  indicates the initial paraelectric phase. (d) Frequency spectrum calculated by performing Fourier transform of the time-domain data in (c) for  $t=10-200$  ps. Polarization profiles showing (e) a zero-energy DW sliding mode and (f) a DW breathing mode, calculated analytically via the eigenmode analysis. (g) Analytically calculated dispersion relation of the soft mode (dashed black curve) and band-folded transverse acoustic phonons (solid lines, colored by the frequency-dependent phonon lifetime). (h) Dispersion relation of coherent polarization wave, represented by  $\langle \Delta P_1 \rangle(k_2, f)$ , calculated by performing 2D Fourier transform of the  $\langle \Delta P_1 \rangle(x_2, t)$  for  $t=100-200$  ps. In (h), the white dashed curve indicates the analytically calculated dispersion of the soft mode.

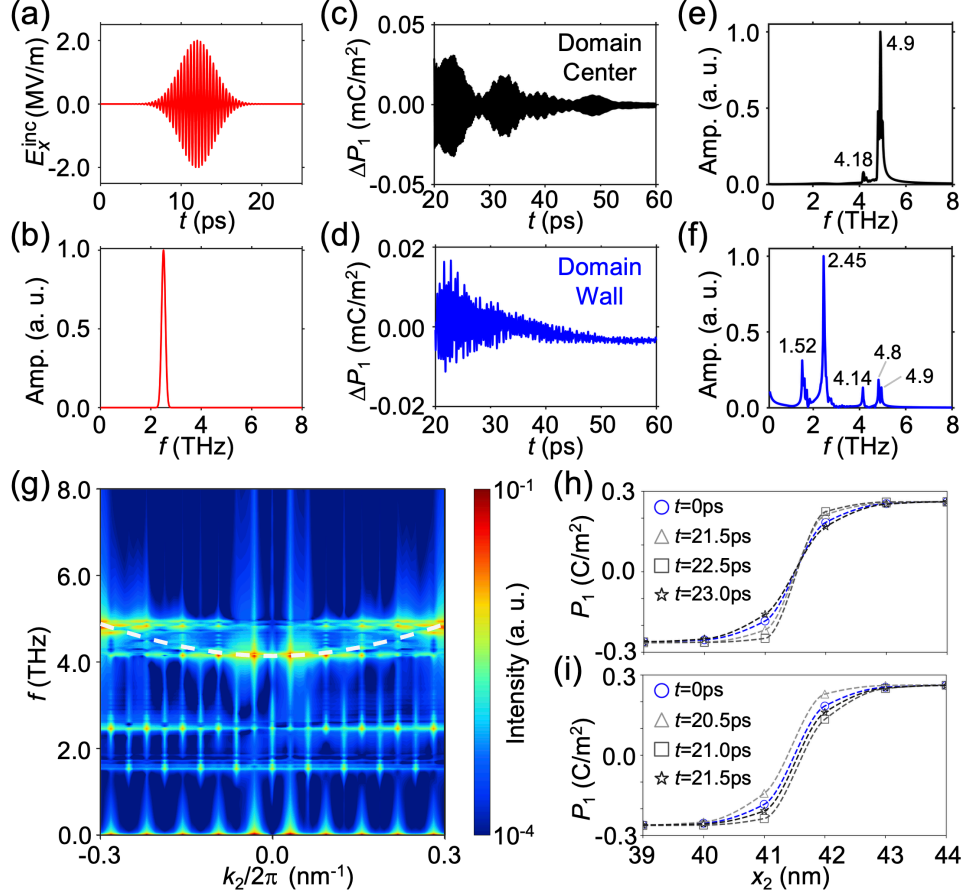


**Fig. 3.** (a) Temporal profile and (b) frequency spectrum of the narrowband 2.5-THz electric-field pulse  $E_x^{\text{inc}}$  applied to the equilibrium stripe domain structure in Fig. 2(a). Evolution of  $\Delta P_1$  at a single point (c) in the center of a domain (i.e., the point at  $x_2=8$  nm along the line in Fig. 2(b)) and (d) at the DW (i.e., the point indicated in Fig. 2(b)). (e,f) Frequency spectra calculated by performing Fourier transforms of the time-domain data in (c) and (d), respectively. (g) Dispersion relation of coherent polarization wave, represented by  $\langle \Delta P_1 \rangle(k_2, f)$ , calculated by performing 2D Fourier transform of the  $\langle \Delta P_1 \rangle(x_2, t)$  for  $t=100-200$  ps. The dashed curves indicate the analytically calculated dispersion of the soft mode. Line profiles of polarization at different time stages, which oscillate at approximately a single temporal frequency of (h) 2.45 THz and (i) 1.52 THz, obtained via the inverse Fourier transform. In (h,i), the markers indicate the raw data points in the reconstructed polarization profile, while the dashed lines are fitted curves.

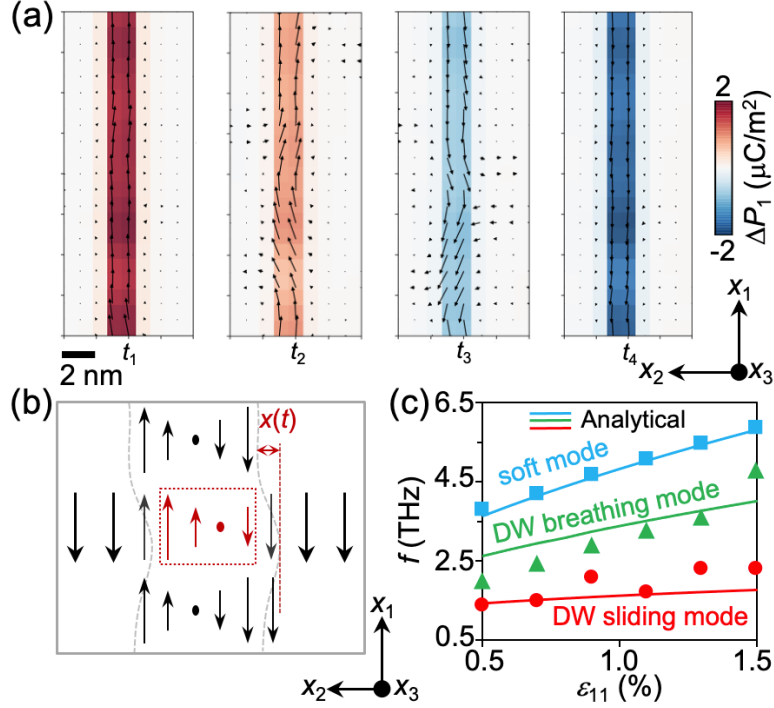


**Figure 4.** (a) 2D distribution of polarization vector reconstructed via the inverse Fourier transform near the frequency of 1.52 THz from the data in Fig. 3 at different time stages, with  $t_1, t_2, t_3, t_4=22.8$  ps, 22.9 ps, 23.0 ps, and 23.1 ps, respectively. The 2D slices show the range of  $x_1=50-70$  nm and  $x_2=22-30$  nm at  $x_3=16$  nm.  $\Delta P_1(t)=P_1(t)-P_1^{\text{eq}}$ . (b) Envisaged physical origin for the unconventional DW sliding mode, where the depolarization field resulting from the polarization discontinuity along the  $x_1$  axis provides a restoring force for the DW sliding along the  $x_2$  axis. (c) Modulation of the resonant frequencies of the DW sliding mode, the DW breathing mode, and the soft mode by strain. The solid lines indicate analytical calculation and the dots indicate the resonant frequencies extracted from dynamical phase-field simulations.

## Appendix A. Dynamical phase-field simulations.

In displacive ferroelectrics, the lattice polarization  $P_i$  is proportional to the coordinates of the soft mode  $Q_j$  (unit: m) via  $P_i = Z_{ij} Q_j$ , where  $Z_{ij} = e_c Z_{ij}^* / V$  is the reduced Born effective charge tensor (typically diagonal) and has a unit of  $C/m^3$ , describing the charge density associated with the soft mode [40].  $Z_{ij}^*$  is the dimensionless Born effective charge,  $e_c$  is the elementary charge, and  $V$  is the volume of unit cell. The subscripts  $i, j = 1, 2, 3$  denote the three orthogonal axes ( $x_1$ - $x_2$ - $x_3$ ) in the crystal physical systems of the parent paraelectric phase. In a dynamical phase-field model, the ferroelectric domain structure is represented by the spatial distribution of  $P_i$  in each discretized cell of the simulation system. The temporal evolution of  $P_i$  is governed by [35,40],

$$\mu_{ij} \frac{\partial^2 P_j}{\partial t^2} + \gamma_{ij} \frac{\partial P_j}{\partial t} = - \frac{\delta F_{\text{tot}}}{\delta P_j}. \quad (\text{A1})$$

Here,  $\mu_{ij} = M_p / (Z_{ij}^2 V)$  is the mass coefficient tensor [73], where  $M_p$  is the effective mass of the soft mode (unit: kg) and  $V$  is the volume of the unit cell.  $\gamma_{ij}$  is the phenomenological damping coefficient. For simplicity, here we consider both  $\mu_{ij} (\equiv \mu)$  and  $\gamma_{ij} (\equiv \gamma)$  to be a scalar quantity, as in previously existing theoretical and computational works (e.g., [35,38,39]).  $F_{\text{tot}}$  is the total Helmholtz free energy of the ferroelectric, which has temperature  $T$ ,  $P_i$ , electric field  $E_i$ , and total strain  $\varepsilon_{ij}$  as the independent (natural) variables. Using  $G_0(T, P_i = 0)$ , i.e., the Gibbs free energy of the ferroelectric under zero  $P_i$ , zero electric field, and zero stress, as the reference,  $F_{\text{tot}}$  can be expressed as,

$$F_{\text{tot}} = \int f_{\text{tot}} dV = \int [f_{\text{Landau}} + f_{\text{elec}} + f_{\text{elas}} + f_{\text{grad}}] dV, \quad (\text{A2})$$

where  $f_{\text{Landau}}$  is the Landau free energy density. For BaTiO<sub>3</sub>, the expression of  $f_{\text{Landau}}$  is provide in [39]. The electrostatic energy density is given by  $f_{\text{elec}} = -\frac{1}{2} \kappa_0 \kappa_b E_i E_j - E_i P_i$ , where the background dielectric permittivity  $\kappa_b$  describes the contribution from the electronic polarization and polarization arising from lattice phonon modes other than soft mode. The electric field  $E_i$  is the sum of the externally applied electric field  $E_i^{\text{inc}}$ , the depolarization field  $E_i^{\text{d}}$ , and the radiating electric field  $E_i^{\text{rad}}$ . Here, the local depolarization field  $E_i^{\text{d}}$  is obtained by numerically solving the electrostatic equilibrium equation  $\nabla \cdot D_i = \nabla \cdot (\kappa_0 \kappa_b E_i^{\text{d}} + P_i(\mathbf{r})) = 0$ , where the effects of long-range electrostatic interaction among the spatially inhomogeneous electric polarization  $P_i(\mathbf{r})$  are incorporated.  $E_i^{\text{rad}}$  is generated by dynamical oscillation of polarization (the polarization current) and can be evaluated by solving the complete set of Maxwell's equations [38,41]. The elastic energy density is expressed as  $f_{\text{elas}} = \frac{1}{2} c_{ijkl} (\varepsilon_{kl} - \varepsilon_{kl}^0) (\varepsilon_{ij} - \varepsilon_{ij}^0)$ , where  $\varepsilon_{ij}$  is the local total strain describing the deformation with respect to the parent paraelectric phase,  $\varepsilon_{ij}^0 = Q_{ijkl} P_k P_l$  is the eigenstrain describing the mechanical deformation arising due to the paraelectric-to-ferroelectric phase transition under zero stress.  $c_{ijkl}$  and  $Q_{ijkl}$  are the elastic stiffness tensor and electrostrictive tensor of the parent paraelectric phase, respectively. The gradient energy density is given by  $f_{\text{grad}} = \frac{1}{2} G_0 (\nabla \mathbf{P})^2$  [74], where  $G_0$  is the isotropic gradient energy coefficient.

To simulate the coupled polarization-strain dynamics in ferroelectric membranes, the dynamical total strain  $\Delta \varepsilon_{ij}(t)$  needs to be considered in calculating  $f_{\text{elas}}$ . We begin by writing the time-varying local total strain  $\varepsilon_{ij}(t) = \varepsilon_{ij}(t=0) + \Delta \varepsilon_{ij}(t)$ . In simulating the ferroelectric domain pattern formation during a paraelectric-to-ferroelectric phase transformation,  $\varepsilon_{ij}(t=0)$  is the local total strain at the initial state ( $t=0$ ), which is a paraelectric phase with a small, randomly

fluctuating polarization magnitude  $|P_i(\mathbf{r}, t=0)| \leq 0.01$  C/m<sup>2</sup>. The resulting eigenstrain in the initial state,  $\varepsilon_{ij}^0(t=0)$ , is therefore small. As a result,  $\varepsilon_{ij}(t=0)$  should be spatially uniform and can be calculated directly based on the mechanical boundary condition. Specifically, for a stress-free ferroelectric membrane, one has  $\varepsilon_{ij}(t=0)=0$  in every cell of the simulation system. For a uniaxially strained membrane where the strain is applied along the  $[100]_c$  axis, the surface tractions along both the  $x_2$  and  $x_3$  axis are zero, i.e.,  $\sigma_{i2} = \sigma_{i3} = 0$  ( $i=1,2,3$ ) [39], one has,

$$\varepsilon_{11}(t=0) = \varepsilon_{11}^{\text{tot}}, \quad (\text{A3a})$$

$$\varepsilon_{12}(t=0) = \varepsilon_{13}(t=0) = \varepsilon_{23}(t=0) = 0, \quad (\text{A3b})$$

$$\varepsilon_{22}(t=0) = \varepsilon_{33}(t=0) = -\frac{c_{12}}{c_{11}+c_{12}} \varepsilon_{11}^{\text{tot}}, \quad (\text{A3c})$$

A knowledge of  $\varepsilon_{ij}(t=0)$  allows us to calculate the initial displacement  $u_i(t=0)$  and the initial stress  $\sigma_{ij}(t=0)$ . The dynamical strain  $\Delta\varepsilon_{ij}(t)$ , which results from the evolving polarization  $P_i(\mathbf{r}, t)$ , can be obtained by solving the elastodynamic equation,

$$\rho \frac{\partial^2 \Delta u_i}{\partial t^2} = \nabla \cdot (\Delta \sigma_{ij} + \beta \frac{\partial \Delta \sigma_{ij}}{\partial t}) \quad (\text{A4})$$

where  $\rho$  is the mass density and  $\beta$  is the elastic damping coefficient.  $\Delta u_i = u_i - u_i(t=0)$  is the dynamical displacement, and  $\Delta \sigma_{ij} = \sigma_{ij} - \sigma_{ij}(t=0)$  is the dynamical stress and can be also written as  $\Delta \sigma_{ij} = c_{ijkl}(\Delta \varepsilon_{kl} - \Delta \varepsilon_{kl}^0)$ , with  $\Delta \varepsilon_{kl}^0 = \varepsilon_{kl}^0 - \varepsilon_{kl}^0(t=0)$  and  $\Delta \varepsilon_{kl} = \frac{1}{2} \left( \frac{\partial \Delta u_k}{\partial l} + \frac{\partial \Delta u_l}{\partial k} \right)$ . Equations (A1) and (A4) are solved in a coupled fashion until the formation of equilibrium ferroelectric domain patterns, where the polarization-changing rate  $\frac{\partial P_i}{\partial t}$ , velocity field  $\frac{\partial u_i}{\partial t}$  and stress-changing rate  $\frac{\partial \sigma_{ij}}{\partial t}$  should all reduce to almost zero. The spatial distributions of  $P_i(\mathbf{r})$ ,  $u_i(\mathbf{r})$ , and  $\sigma_{ij}(\mathbf{r})$  corresponding to the equilibrium ferroelectric domain can then be used as the initial condition for the new simulations, for example, the excitation of the equilibrated ferroelectric domains by an applied electric-field pulse or other external stimuli (e.g., temperature, stress fields).

In 3D simulations, discretized cells of  $N_1 \Delta x_1 \times N_2 \Delta x_2 \times N_3 \Delta x_3$ , with a cell size of  $\Delta x_1 = \Delta x_2 = \Delta x_3 = 1$  nm and  $(N_1, N_2, N_3) = (128, 128, 32)$ , are used to describe the ferroelectric nanomembrane. Additional vacuum layers, each having a thickness of 10 cells, are added around the ferroelectric membrane except those along the axis of the applied strain (i.e., the  $x_1$  axis). The electrostatic equilibrium equation ( $\nabla \cdot D_i = 0$ ) is numerically solved by the Fourier Spectral Iterative Perturbation method [75], which requires the application of periodic boundary condition to all six surfaces of the system. A large  $\kappa_b$  of  $>10^5$  is assigned to the vacuum layers while we set  $\kappa_b = 5$  for the ferroelectric BTO membrane [41]. As a result, the polarization charges at the  $x_1$ - $x_2$  and  $x_1$ - $x_3$  plane surfaces are fully compensated, which in practice could occur by the accumulation of mobile ionic/electronic defects at the surfaces. The equation of motion for the polarization (Eq. (A1)) and the dynamical displacement (Eq. (A4)) are both solved in real-space, where a classical Runge-Kutta method is used for the time marching using a dimensionless time step of  $\Delta t = 5.0 \times 10^{-15}$  s, and the central finite-difference is used to calculate the spatial derivatives in the calculation of the thermodynamic driving force resulting from the  $f_{\text{grad}}$ . Our control simulations show that halving the  $\Delta t$  does not alter the equilibrium ferroelectric domain structure. The Neumann boundary condition  $\partial P_i / \partial \mathbf{n} = 0$  [41] is applied to the membrane/air interface in solving Eq. (14). Stress continuity condition,  $\boldsymbol{\sigma}^A \cdot \mathbf{n} = \boldsymbol{\sigma}^B \cdot \mathbf{n}$ , is applied all membrane/vacuum interfaces in solving Eq. (A4), where the superscripts ‘A’ and ‘B’ denote different materials and  $\mathbf{n}$  is the interface normal. By using a negligibly small  $c_{ijkl}$  ( $\sim 1$  Pa) for the vacuum layer, the mechanical boundary condition

of zero surface traction along both the  $x_2$  and  $x_3$  axis are automatically satisfied. In simulating the equilibrium domain pattern [Figs. 1(a), 2(a), and 6(a)], the total number of numerical time steps is set to 60,000, which is sufficiently large to ensure the system has reached the thermodynamic equilibrium. All the real-space and Fourier-space numerical solvers are accelerated through graphics processing unit (GPU) parallelization.

The material parameters for performing dynamical phase-field simulations of ferroelectric BTO are summarized in [35,38,76,77]. The calculated free energy density profile [Fig. 1(b)] is a sum of  $f_{\text{Landau}}$  and  $f_{\text{elas}}$  by setting  $P_2=P_3=0$ , a spatially uniform  $P_1$ , and a fixed total strain  $\varepsilon_{ij}=\varepsilon_{ij}^0(P=P_i^{\text{eq}})$ , where  $P_i^{\text{eq}}$  is the equilibrium polarization that can be obtained by minimizing the sum of  $f_{\text{Landau}}$ ,  $f_{\text{elec}}$ , and  $f_{\text{elas}}$  under the electric and mechanical boundary conditions described above. For BaTiO<sub>3</sub>, the Landau parameters in  $f_{\text{Landau}}$  are [77]:  $\alpha_1=4.124 \times 10^5(T - 388) \text{ N}\cdot\text{m}^2\cdot\text{C}^{-2}$ ,  $\alpha_{11}=-2.097 \times 10^8 \text{ N}\cdot\text{m}^6\cdot\text{C}^{-4}$ ,  $\alpha_{12}=7.974 \times 10^8 \text{ N}\cdot\text{m}^6\cdot\text{C}^{-4}$ ,  $\alpha_{111}=1.294 \times 10^9 \text{ N}\cdot\text{m}^{10}\cdot\text{C}^{-6}$ ,  $\alpha_{112}=-1.950 \times 10^9 \text{ N}\cdot\text{m}^{10}\cdot\text{C}^{-6}$ ,  $\alpha_{123}=-2.500 \times 10^9 \text{ N}\cdot\text{m}^{10}\cdot\text{C}^{-6}$ ,  $\alpha_{1111}=3.863 \times 10^{10} \text{ N}\cdot\text{m}^{14}\cdot\text{C}^{-8}$ ,  $\alpha_{1112}(\text{N}\cdot\text{m}^{14}\cdot\text{C}^{-8})=2.529 \times 10^{10} \text{ N}\cdot\text{m}^{14}\cdot\text{C}^{-8}$ ,  $\alpha_{1122}=1.637 \times 10^{10} \text{ N}\cdot\text{m}^{14}\cdot\text{C}^{-8}$ ,  $\alpha_{1123}=1.367 \times 10^{10} \text{ N}\cdot\text{m}^{14}\cdot\text{C}^{-8}$ . The elastic stiffness coefficient and the electrostrictive coefficients are (in Voigt notation) [76]:  $c_{11}=178 \text{ GPa}$ ,  $c_{12}=96.4 \text{ GPa}$ ,  $c_{44}=122 \text{ GPa}$ ,  $Q_{11}=0.1 \text{ m}^4\cdot\text{C}^{-2}$ ,  $Q_{12}=-0.034 \text{ m}^4\cdot\text{C}^{-2}$ ,  $Q_{44}=0.029 \text{ m}^4\cdot\text{C}^{-2}$ . The isotropic gradient energy coefficient is set to be  $G_0=1.0 \times 10^{-10} \text{ C}^{-2}\cdot\text{m}^4\cdot\text{N}$ . The polarization damping coefficient  $\gamma$  is  $2 \times 10^{-7} \text{ }\Omega\cdot\text{m}$  [38], which is set to the same as the value for PbTiO<sub>3</sub> [28]. The elastic damping coefficient  $\beta$  is  $6 \times 10^{-12} \text{ s}$  [35].

## Appendix B. Analytical calculation of the dispersion relation of transverse polarization waves in single-domain ferroelectrics

Let us consider a single-domain BTO nanomembrane with an initial equilibrium (spontaneous) polarization  $P_1^{\text{eq}}$  along the  $x_1$  axis, as shown in Fig. 1(a). The frequency-wavenumber ( $\omega$ - $\mathbf{k}$ ) dispersion relation of coherent polarization waves in such single-domain BTO can be obtained by linearizing Eq. (A1). As an example, we study the dispersion relation of the transverse coherent polarization wave,  $\Delta P_1(x_2, t)$ , which also corresponds to the ferroelectric soft mode (a transverse optical phonon [53]). Assuming  $\gamma=0$ ,  $E_i^{\text{inc}}=0$ ,  $E_i^{\text{d}}=0$ , and  $E_i^{\text{rad}}=0$ , and performing Taylor expansion for the functional derivative on the right, Eq. (A1) reduces to,

$$\mu \frac{\partial^2 P_1}{\partial t^2}(x_2, t) = G_0 \nabla^2 P_1(x_2, t) - K \Delta P_1 - \frac{1}{2} C (\Delta P_1)^2 \dots, \quad (\text{B1})$$

where the pre-factors in the Taylor expansion are calculated as  $K = \partial^2 f_{\text{tot}} / \partial P_1^2$  and  $C = \partial^3 f_{\text{tot}} / \partial P_1^3$ . Keeping only the linear terms and plugging in the plane-wave solution for the transverse polarization wave, i.e.,  $P_1(x_2, t) = P_1^{\text{eq}} + \Delta P_1 = P_1^{\text{eq}} + \Delta P_1^0 e^{i(k_2 x_2 - \omega t)}$ , one has,

$$(-\mu \omega_t^2 + G_0 k_2^2 + K) \Delta P_1 = 0, \quad (\text{B2})$$

Rewriting Eq. (B2) lead to the dispersion relation of the soft mode, given by,

$$\omega_t^2 = \omega_0^2 + \frac{G_0}{\mu} k_2^2, \quad (\text{B3})$$

where  $\omega_0 = \sqrt{K/\mu}$  is the soft mode frequency at  $k_2 = 0$ .

### Appendix C. Theoretical analyses of the bound-state modes at the domain walls

We consider a 1D Ising-type 180° DW under the conditions of  $\lim_{x_2 \rightarrow \pm\infty} P_1(x_2) = \pm |P_1^{0,\text{eq}}|$ , where  $|P_1^{\text{eq}}|$  is the magnitude of equilibrium polarization in the domain center and should be the same as those in a single-domain ferroelectric.  $|P_1^{\text{eq}}| = 0.26$  C/m<sup>2</sup> when  $\varepsilon_{11} = 0.7\%$ . The value of  $|P_1^{\text{eq}}|$  under other strains can be determined by minimizing the total free energy of a single-domain ferroelectric. The equilibrium polarization profile across the DW,  $P_1^{\text{eq}}(x_2)$ , can be obtained by numerically solving the 1D Euler-Lagrange equation,

$$\frac{\delta F_{\text{tot}}}{\delta P_1} = \frac{\partial(f^{\text{Landau}} + f^{\text{Elas}})}{\partial P_1} - G_0 \frac{\partial^2 P_1}{\partial x_2^2} = 0. \quad (\text{C1})$$

The numerically solved profile,  $P_1^{\text{eq}}(x_2)$ , is shown in Figs. 1(e,f), and can be fitted using  $P_1^{\text{eq}}(x_2) = |P_1^{0,\text{eq}}| \varphi\left(\frac{x_2 - X}{W}\right)$ , where  $X$  denotes the coordinates of the DW center and  $W$  is the DW width. The shape function  $\varphi(\xi)$  satisfies the conditions of  $\lim_{\xi \rightarrow \pm\infty} \varphi(\xi) = \pm 1$  and  $\varphi(0) = 0$ .

Dynamical evolution of the DW profile,  $P_1(x_2, t)$ , is governed by the equation of motion for the lattice polarization [Eq. (A1)], which is written as follows for the present 1D system,

$$\mu \frac{\partial^2 P_1(x_2, t)}{\partial t^2} + \gamma \frac{\partial P_1(x_2, t)}{\partial t} = - \frac{\delta F_{\text{tot}}}{\delta P_1(x_2, t)}. \quad (\text{C2})$$

Substituting the relation  $P_1(x_2, t) = P_1^{\text{eq}}(x_2) + \delta P_1(x_2, t)$  into Eq. (C2) and setting  $\gamma = 0$  allows us to linearize the equation and rewrite Eq. (C2) into the following perturbation form,

$$\frac{\partial^2 \delta P_1(x_2, t)}{\partial t^2} = \mathcal{H} \delta P_1(x_2, t), \quad (\text{C3})$$

where the operator  $\mathcal{H} = \frac{G_0}{\mu} \frac{\partial^2}{\partial x_2^2} - \frac{1}{\mu} U(x_2)$ ,  $U(x_2) = \left. \frac{\partial^2(f^{\text{Landau}} + f^{\text{Elas}})}{\partial P_1^2} \right|_{P_1 = P_1^{\text{eq}}(x_2)}$  denotes the local curvature at the equilibrium polarization profile  $P_1^{\text{eq}}(x_2)$ . The solution to Eq. (C3) can be expanded in terms of the normal modes  $\psi_n(x_2)$ ,

$$\delta P_1(x_2, t) = \sum_n a_n \psi_n(x_2) e^{-i\omega_n t}, \quad (\text{C4})$$

where  $\psi_n(x_2)$  and resonant frequencies  $\omega_n$  are, respectively, the eigenfunctions and the eigenfrequencies that can be obtained from solving the eigenvalue problem, i.e.,

$$\mathcal{H} \psi_n(x_2) = -\omega_n^2 \psi_n(x_2), \quad (\text{C5})$$

To numerically solve Eq. (C5), the operator  $\mathcal{H}$  is first discretized along the wall-normal direction  $x_2$  using a uniform grid with a size  $\Delta x_2 = 0.02$  nm. The second spatial derivative in the operator  $\mathcal{H}$  is approximated by a centered finite-difference scheme, resulting in a tridiagonal real-symmetric matrix representation of  $\mathcal{H}$ . After this discretization, Eq. (C5) is transformed into a standard matrix eigenvalue problem,

$$\mathcal{H}\vec{\psi}_n = \lambda_n\vec{\psi}_n, \omega_n^2 = -\lambda_n \quad (\text{C6})$$

where  $\vec{\psi}_n$  is the discrete sampling of  $\psi_n(x_2)$ . Dirichlet boundary conditions, i.e.,  $\psi_n(x_2)=0$ , are applied to both ends of the 1D simulation system to represent the rigid domains ( $\delta P_1(x_2, t) = 0$ ) on either side of the domain wall. The tridiagonal matrix  $\mathcal{H}$  is then diagonalized using standard symmetric eigensolvers, which directly yield the eigenvalues  $\lambda_n$  and the corresponding normalized eigenvectors  $\vec{\psi}_n$ . The eigenfrequencies follow the relation  $\omega_n^2 = -\lambda_n$ , and the eigenvectors provide the spatial mode profiles of the domain-wall collective oscillations.

## Appendix D. Dispersion relation and lifetime of the band-folded acoustic phonons.

*Dispersion relation.* The acoustic waves in the periodic domain structure can be reflected at the domain walls due to the discontinuity in the electromechanical impedance between two ferroelectric domains that are oppositely poled, leading to opposite piezoelectric tensors, but otherwise have identical mechanical properties [78]. This discontinuity results in a dispersion band-folding in the momentum space. Let us consider the propagation of a transverse acoustic (TA) wave in a 1D system with equilibrium polarization along the  $\pm x_1$  axis and a domain periodicity along the  $x_2$  axis. The velocity of TA wave is  $v_t = \sqrt{c_{44}/\rho}$ , where  $c_{44}$  is the elastic stiffness coefficient (Voigt notation) of the ferroelectric. The TA wave can be expressed by a combination of two plane waves propagating along  $+x_2$  and  $-x_2$  direction,

$$u_1(x_2, t) = u_1^+ e^{i(k_t x_2 - \omega_t t)} + u_1^- e^{i(-k_t x_2 - \omega_t t)}, \quad (\text{D1})$$

where  $k_t = \omega_t/v_t$  is the angular wavenumber of the TA waves within each domain period and  $\omega_t$  is the corresponding angular frequency. The elastic stress components for the cubic BaTiO<sub>3</sub> system are then calculated as,

$$\begin{pmatrix} \sigma_{11} \\ \sigma_{22} \\ \sigma_{33} \\ \sigma_{23} \\ \sigma_{13} \\ \sigma_{12} \end{pmatrix} = \begin{bmatrix} c_{11} & c_{12} & c_{12} & 0 & 0 & 0 \\ c_{12} & c_{11} & c_{12} & 0 & 0 & 0 \\ c_{12} & c_{12} & c_{11} & 0 & 0 & 0 \\ 0 & 0 & 0 & c_{44} & 0 & 0 \\ 0 & 0 & 0 & 0 & c_{44} & 0 \\ 0 & 0 & 0 & 0 & 0 & c_{44} \end{bmatrix} \begin{pmatrix} e_{11} \\ e_{22} \\ e_{33} \\ 2e_{23} \\ 2e_{13} \\ 2e_{12} \end{pmatrix}, \quad (\text{D2})$$

where  $e_{ij} = \frac{1}{2} \left( \frac{\partial u_i}{\partial x_j} + \frac{\partial u_j}{\partial x_i} \right)$  are the elastic strain components,  $c_{ij}$  are the elastic stiffness constants.

In a 1D system that only hosts a TA wave,  $u_1(x_2, t)$ , the only nonzero stress component is,

$$\sigma_{12} = c_{44} \frac{\partial u_1}{\partial x_2}, \quad (\text{D3})$$

The periodic boundary conditions of both displacement  $u_1$  and stress  $\sigma_{12}$  are expressed as [79]:

$$u_1(x_2 = 0) = u_1(x_2 = d) e^{iK_t d}, \quad (\text{D4})$$

$$\sigma_{12}(x_2 = 0) = \sigma_{12}(x_2 = d) e^{iK_t d}, \quad (\text{D5})$$

where  $D$  is the domain periodicity (the thickness of one domain along the  $x_2$  axis) and  $K_t$  is the effective (superlattice) wavevector which defines the folded Brillouin zone  $-\pi/D \leq K_t \leq \pi/D$ . Plugging in Eqs. (D1,D3) into Eqs. (D4-D5) yields the following equations written in matrix form,

$$\begin{bmatrix} 1 - e^{id(K_t + \frac{\omega_t}{v_t})} & 1 - e^{id(K_t - \frac{\omega_t}{v_t})} \\ ic_{44} \frac{\omega_t}{v_t} (1 - e^{id(K_t + \frac{\omega_t}{v_t})}) & ic_{44} \frac{\omega_t}{v_t} (-1 + e^{id(K_t - \frac{\omega_t}{v_t})}) \end{bmatrix} \begin{bmatrix} u_1^+ \\ u_1^- \end{bmatrix} = 0. \quad (\text{D6})$$

Obtaining non-trivial solution for Eq. (D6) requires that the determinant of the coefficient matrices to be zero, which gives rise to the resonant condition for the TA standing waves,

$$\cos(dK_t) = \cos\left(d \frac{\omega_t}{v_t}\right). \quad (\text{D7})$$

Thus, the dispersion relation of TA standing waves are given by,

$$\omega_t = \left( K_t + n \frac{2\pi}{d} \right) v_t, \quad (\text{D8})$$

where integer  $n$  indicates multiple band-folding in the momentum space. We note that the dispersion relations above show that all frequencies are allowed, suggesting the absence of frequency band gaps. This is consistent with the fact that there is no acoustic impedance mismatch between two adjacent domains that have the same sound velocity and mass density.

*Lifetime.* The dissipation rate of the acoustic modes characterizes their lifetime. The dissipation rate of acoustic phonons is related to the imaginary component of the linear acoustic susceptibility that can be derived from the linearization of the elastodynamic equation, given by,

$$\rho \frac{\partial^2 u_i}{\partial t^2} = \nabla \cdot \left( \sigma_{ij} + \beta \frac{\partial \sigma_{ij}}{\partial t} \right) + f, \quad (\text{D10})$$

where  $\beta$  is the elastic damping coefficient,  $f$  is the externally applied volumetric force. By writing  $u_1(x_2, t) = u_1 e^{i(k_t x_2 - \omega_t t)}$  under the plane-wave assumption and  $f = f_0 e^{-i\omega_t t}$ , one can derive the frequency-domain equations governing the propagation of TA waves,

$$-\rho \omega_t^2 u_1(x_2) = -c_{44}(1 - \mathbf{i}\beta\omega_t)k_t^2 u_1(x_2) + f. \quad (\text{D11})$$

Re-arranging Eq. (D11) allows for deriving the acoustic susceptibility, given by,

$$\chi_t = \frac{u_1(\omega_t)}{f(\omega_t)} = \frac{1}{c_{44}(1 - \mathbf{i}\beta\omega_t)k_t^2 - \rho\omega_t^2}. \quad (\text{D12})$$

The dissipation rate  $\kappa$  is proportional to the imaginary part of the susceptibility:  $\kappa_t \propto \omega_t^2$ , whereas the acoustic mode lifetime is inversely proportional to the dissipation rate  $\kappa$ , i.e.,  $\tau_t \propto \frac{1}{\omega_t^2}$ .

## Appendix E: Polarization profile/distribution reconstructed at a target frequency

To obtain the line profiles in Figs. 3(h,i), we first select a line profile along the  $x_2$  axis (i.e., the dashed line in Fig. 2(a)) to extract the raw simulation data  $P_1(x_2, t)$ . The Fourier analysis of this raw data gives the frequency spectrum for all the points along the selected line  $\tilde{P}_1(x_2, f)$ . This intensity spectrum consists of multiple frequency peaks and includes all the dynamical components. To reconstruct the spatial profile of polarization oscillating at a target frequency  $f_0$ ,  $\Delta P_1(x_2, t)$ , we perform the inverse Fourier transform for the intensity spectrum  $\tilde{P}_1(x_2, f_0 - \Delta f < f < f_0 + \Delta f)$  at the target frequency peak with a selected bandwidth of  $\pm\Delta f$ . For better visualization, the reconstructed line profiles are plotted as  $P_1^{\text{eq}}(x_2) + A\Delta P_1(x_2, t)$ , where  $P_1^{\text{eq}}(x_2)$  is the initial equilibrium polarization profile at  $t = 0$ , and the pre-factor  $A$  is used to amplify the amplitude of polarization wave. Specifically, we set  $A=3\times 10^4$  in Figs. 3(h,i).

Similarly, to reconstruct the 2D polarization distribution, we first select a 2D slice in the  $x_1$ - $x_2$  plane and reconstruct both the  $\Delta P_1(x_1, x_2, t)$  and  $\Delta P_2(x_1, x_2, t)$  components using the inverse Fourier transform method described above. By plotting the reconstructed polarization distribution in the  $x_1$ - $x_2$  using vectors whose lengths indicate the amplitude of the polarization oscillation, we obtain the 2D distribution of polarization vector for the mode oscillating at the target frequency. The results for the unconventional DW sliding mode are shown in Fig. 4(a). The results for the DW breathing mode are shown in Fig. 5 below.

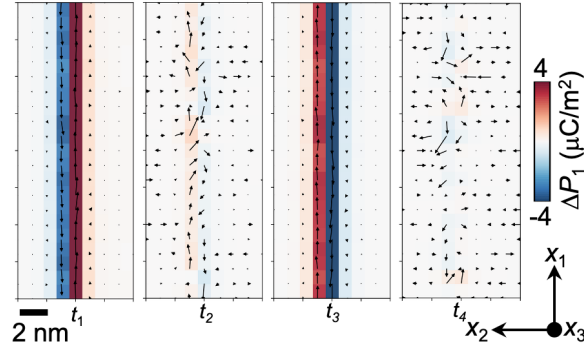


**Figure 5.** 2D distribution of polarization vector reconstructed via the inverse Fourier transform near the frequency of 2.45 THz from the data in Fig. 3 at different time stages, with  $t_1, t_2, t_3, t_4 = 22.8$  ps, 22.9 ps, 23.0 ps, and 23.1 ps, respectively. The 2D slices show the range of  $x_1 = 50-70$  nm and  $x_2 = 22-30$  nm at  $x_3 = 16$  nm.  $\Delta P_1(t) = P_1(t) - P_1^{\text{eq}}$ .

## Appendix F. Analytical model for the unconventional DW sliding mode

We consider the case in which both the polarization oscillation and the wavevector are aligned along the  $x_1$  axis. In this case, the longitudinal modulation of polarization generates a bulk bound charge density, which in turn produces a depolarization field along the  $x_1$  axis. This depolarization field acts as a restoring force when the domain wall is displaced from its equilibrium position, as shown in Fig. 4(c). To calculate the resonance frequency of this wavy DW sliding mode, we develop a harmonic oscillator model by analogy to that reported in [62], with an equation of motion written as,

$$\mu_{\text{DW}} \frac{\partial^2 x(t)}{\partial t^2} + \gamma_{\text{DW}} \frac{\partial x(t)}{\partial t} + k_{\text{DW}} x(t) = 0, \quad (\text{F1})$$

where  $x(t)$  denotes the DW displacement along the  $x_2$  axis with respect to the equilibrium location (unit: m),  $\mu_{\text{DW}}$  is the DW mass density (unit: kg/m<sup>2</sup>),  $\gamma_{\text{DW}}$  is the damping coefficient (unit: kg/m<sup>2</sup>/s), and  $k_{\text{DW}}$  is the spring constant (unit: kg/m<sup>2</sup>/s<sup>2</sup>) which is associated with the areal potential energy  $\Delta U$  (unit: J/m<sup>2</sup>).  $\Delta U$  is written as,

$$\Delta U = \frac{1}{2} k_{\text{DW}} x(t)^2, \quad (\text{F2})$$

Physically,  $\Delta U$  originates from the local electrostatic energy penalty from the depolarization field along  $E_1^{\text{d}}$ . Therefore,  $\Delta U$  can be calculated by integrating the local electrostatic energy density,  $-\frac{1}{2} E_1^{\text{d}}(x_2) P_1(x_2)$  along the  $x_2$  axis, i.e.,

$$\Delta U = \int_{-\frac{W}{2}+x}^{\frac{W}{2}} -\frac{1}{2} E_1^{\text{d}} P_1(x_2 - x) dx_2, \quad (\text{F3})$$

To simplify the calculation, we consider the polarization profile across the DW is approximately described by the following function,

$$P_1(x_2) \approx \begin{cases} -P_1^{0,\text{eq}}, & x_2 < -\frac{W}{2} \\ \frac{P_1^{0,\text{eq}}}{W} x_2, & -\frac{W}{2} \leq x_2 \leq \frac{W}{2} \\ P_1^{0,\text{eq}}, & x_2 \geq \frac{W}{2} \end{cases} \quad (\text{F4})$$

The depolarization field can be written as  $E_1^{\text{d}} = -\frac{\delta P_1}{\kappa_0 \kappa_{\text{b}}}$ , where  $\delta P_1$  denotes the bulk bound charge density along the  $x_1$  axis, resulting from the displacement  $x(t)$ .  $\delta P_1$  can be approximately calculated based on  $x(t)$ , given by,

$$\delta P_1 \approx -\frac{2P_1^{0,\text{eq}}}{W} x(t). \quad (\text{F5})$$

Equation (F5) indicates that a positive DW displacement  $x(t)$  will induce a negative  $\delta P_1$  at the DW, which is consistent with the results in Fig. 3(i). Substituting Eqs. F(4, 5) into Eq. (F3),  $\Delta U$  can be written as,

$$\Delta U \approx \frac{P_1^{0,\text{eq}^2} x(t)^2}{W^2 \kappa_0 \kappa_{\text{b}}} (W - x(t)). \quad (\text{F6})$$

Equation (F6) shows that both a positive and a negative DW displacement  $x(t)$  increases the areal potential energy electrostatic energy by  $\Delta U$ . If assuming  $W \gg x(t)$ , one can further derive the spring constant  $k_{\text{DW}}$  as,

$$k_{\text{DW}} = \frac{d^2 \Delta U}{dx^2} \approx \frac{2P_1^{0,\text{eq}^2}}{\kappa_0 \kappa_b W}, \quad (\text{F7})$$

A knowledge of  $k_{\text{DW}}$  allows for calculating the resonance frequency of DW sliding,

$$\omega_{\text{DW}} = \sqrt{\frac{k_{\text{DW}}}{\mu_{\text{DW}}}} = \sqrt{\frac{2P_1^{0,\text{eq}^2}}{\mu_{\text{DW}} \kappa_0 \kappa_b W}}, \quad (\text{F8})$$

For the case of  $\varepsilon_{11}=0.7\%$ , one has  $P_1^{\text{eq}}=0.26 \text{ C/m}^2$  and  $W \approx 1.67 \text{ nm}$ . Using  $\omega_{\text{DW}}/2\pi=1.52 \text{ THz}$  from the dynamical phase-field simulations,  $\mu_{\text{DW}}$  is calculated to be  $2.02 \times 10^{-8} \text{ kg/m}^2$ . By assuming  $\mu_{\text{DW}}$  does not change with strain, we can then analytically calculate the  $\omega_{\text{DW}}$  under other strain values.

## Appendix G. Temperature-strain stability phase diagram of uniaxially strained BaTiO<sub>3</sub> membrane.

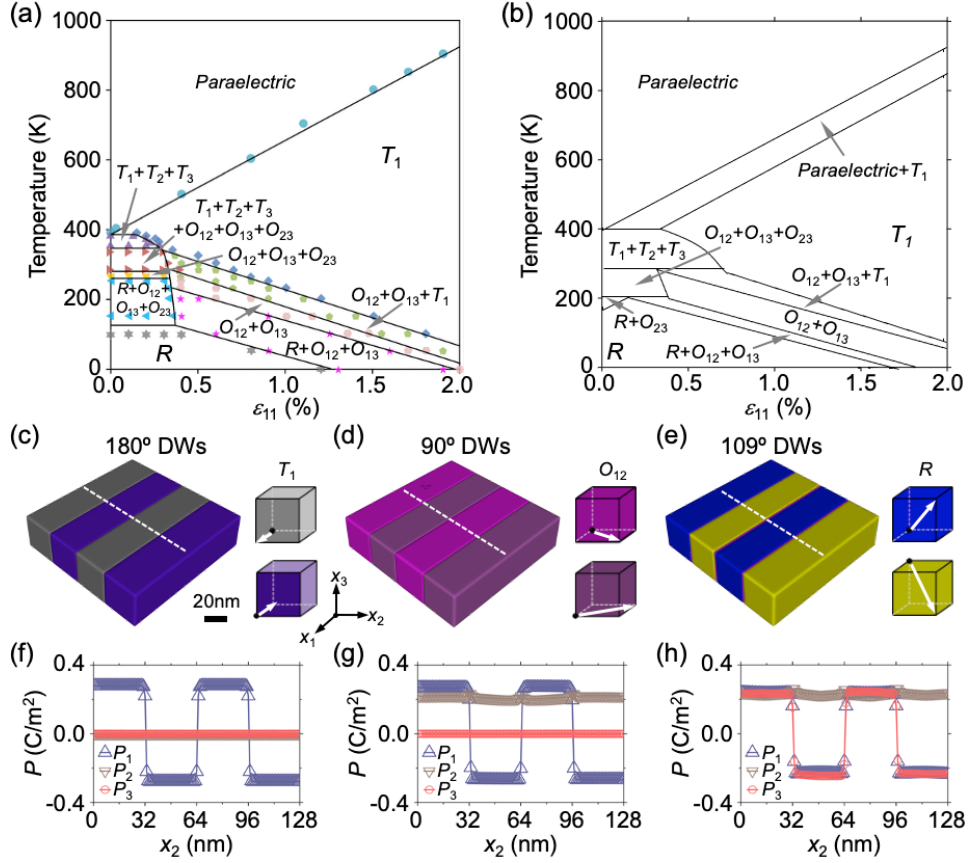


**Fig. 6.** The temperature-uniaxial strain stability phase diagram of multidomain structures of the BTO membrane from (a) dynamical phase-field simulations and (b) analytical calculations. (c,d,e) Typical striped domain structures of the BTO membrane obtained under uniaxial strain of 1.0% at 300 K (c), 0.7% at 200 K (d), and 0.2% at 100 K (e), from the phase diagram in (a). The initial polarization distributions were defined as follows: for 180° DW, opposite  $\pm P_1$  domains with  $P_2=P_3=0$ ; for 90° DW, alternating  $P_1$  while keeping  $P_2$  uniform ( $P_3=0$ ); for 109° DW, opposite  $P_1$  and  $P_3$  while  $P_2$  remained uniform between domains. In all cases, the initial  $|P_i|$  were assigned within  $0.01 \text{ C/m}^2$  to provide small perturbations for domain evolution. (f,g,h) The spatial profiles of the polarization components  $P_1$ ,  $P_2$ , and  $P_3$  along the dashed lines in (c-e), corresponding to the 180°, 90°, and 109° DWs, respectively.

Figure 6(a) shows the temperature-uniaxial strain stability diagram of multiple polar phases (domain states) in a 32-nm-thick BTO nanomembrane obtained by dynamical phase-field simulations (see Appendix A). As temperature decreases, the membrane undergoes a cubic (paraelectric)-tetragonal( $T$ )-orthorhombic( $O$ )-rhombohedral ( $R$ ) transition, similarly to the bulk BTO single crystals. At large  $\varepsilon_{11}$ , the  $T_1$  phase (with a spontaneous polarization aligning along the  $x_1$  axis) is stabilized. Figures 6(c-e) show the representative domain structures of  $T$ -,  $O$ -, and  $R$ -dominant phase under different temperatures and strain combinations with 180°, 90°, and 109° DW, and their corresponding line profiles of polarization are shown in Fig. 6(f-h), respectively. Figure 6(b) shows the phase diagram predicted by extending the thermodynamic theory of strain phase

separation reported in [80] to incorporate the mechanical boundary condition of a uniaxially strained membrane (see details below). This analytically calculated diagram reproduces the key features observed in phase-field simulations, including the locations of phase stability regions and the temperature-dependent slopes of phase boundaries. However, notable discrepancies arise in the stability of multiphase regions. Because the thermodynamic theory neglects the energetic cost of spatial inhomogeneities, such as domain walls and the effects of inhomogeneous  $\mathbf{P}$  on the local total strain and depolarization field, it tends to overestimate the stability window of multidomain configurations. For instance, the strain phase-separation model predicts the  $(T_1+T_2+T_3)/T_1$  phase boundary near 0.65% strain at 300 K, whereas phase-field simulations place the boundary closer to 0.4% strain. In some cases, the inclusion of spatial inhomogeneity energy in the phase-field model eliminates entire phase regions predicted by the thermodynamic approach. One such example is the paraelectric +  $T_1$  region, which appears in the strain phase-separation calculations but is absent in the phase-field results. Such agreements and the explainable discrepancies together corroborate the thermodynamical consistency of the equilibrium ferroelectric domain structures predicted by dynamical phase-field simulations.

*Analytical calculation of the temperature-uniaxial strain stability diagram for membranes*

We start from the Gibbs free energy density function under constant temperature and stress conditions,

$$\begin{aligned}
g(T, P_i, \sigma_{ij}) = & \alpha_1(P_1^2 + P_2^2 + P_3^2) + \alpha_{11}(P_1^4 + P_2^4 + P_3^4) + \alpha_{12}(P_1^2 P_2^2 + P_2^2 P_3^2 + P_1^2 P_3^2) \\
& + \alpha_{111}(P_1^6 + P_2^6 + P_3^6) + \alpha_{112}(P_1^2(P_2^4 + P_3^4) + P_2^2(P_1^4 + P_3^4) + P_3^2(P_1^4 + P_2^4)) + \\
& \alpha_{123}(P_1^2 P_2^2 P_3^2) + \alpha_{1111}(P_1^8 + P_2^8 + P_3^8) + \alpha_{1112}[P_1^6(P_2^2 + P_3^2) + P_2^6(P_1^2 + P_3^2) + P_3^6(P_1^2 + \\
& P_2^2)] + \alpha_{1122}(P_1^4 P_2^4 + P_2^4 P_3^4 + P_1^4 P_3^4) + \alpha_{1123}(P_1^4 P_2^2 P_3^2 + P_2^4 P_1^2 P_3^2 + P_3^4 P_2^2 P_1^2) \\
& - \frac{1}{2} S_{11}(\sigma_{11}^2 + \sigma_{22}^2 + \sigma_{33}^2) - S_{12}(\sigma_{11}\sigma_{22} + \sigma_{22}\sigma_{33} + \sigma_{33}\sigma_{11}) - \frac{1}{2} S_{44}(\sigma_{12}^2 + \sigma_{23}^2 + \sigma_{31}^2) \\
& - Q_{11}(\sigma_{11}P_1^2 + \sigma_{22}P_2^2 + \sigma_{33}P_3^2) - Q_{12}(\sigma_{11}(P_2^2 + P_3^2) + \sigma_{22}(P_1^2 + P_3^2) + \sigma_{33}(P_1^2 + P_2^2)) \\
& - Q_{44}(\sigma_{23}P_2P_3 + \sigma_{13}P_1P_3 + \sigma_{12}P_1P_2), \tag{G1}
\end{aligned}$$

where  $S_{11}$ ,  $S_{12}$ , and  $S_{44}$  are elastic compliance coefficients. Next, we perform the Legendre transform to convert to a modified Helmholtz free energy, going from constant stress to a uniaxially strained conditions,

$$\tilde{f}(T, P_i, \varepsilon_{11}, \sigma_{ij}_{(ij \neq 11)}) = f(T, P_i, \sigma_{ij}) + \varepsilon_{11}\sigma_{11}, \tag{G2}$$

where the total strain  $\varepsilon_{11}$  can be derived via the relation,

$$\varepsilon_{11} = - \left( \frac{\partial f}{\partial \sigma_{11}} \right)_{T, P_i, \sigma_{ij}_{(ij \neq 11)}} = Q_{11}P_1^2 + Q_{12}(P_2^2 + P_3^2) + S_{11}\sigma_{11} + S_{12}(\sigma_{22} + \sigma_{33}). \tag{G3}$$

Re-writing Eq. (G3) leads to,

$$\sigma_{11} = \frac{\varepsilon_{11} - Q_{11}P_1^2 - Q_{12}(P_2^2 + P_3^2) - S_{12}(\sigma_{22} + \sigma_{33})}{S_{11}}. \tag{G4}$$

Substituting Eq. (G4) into Eq. (G2), and setting  $\sigma_{ij(ij \neq 11)} = 0$  (or equivalently,  $\sigma_{i2} = \sigma_{i3} = 0$ , see also Eqs. (A3a-c)) based on the mechanical boundary condition of the uniaxially strained membrane, the modified Helmholtz free energy can be expanded into,

$$\begin{aligned} \tilde{f}(T, P_i, \varepsilon_{11}, \sigma_{ij(ij \neq 11)} = 0) &= a_1(P_1^2 + P_2^2 + P_3^2) + a_{11}(P_1^4 + P_2^4 + P_3^4) + a_{12}(P_1^2 P_2^2 + P_2^2 P_3^2 + P_1^2 P_3^2) \\ &+ a_{111}(P_1^6 + P_2^6 + P_3^6) + a_{112}(P_1^2(P_2^4 + P_3^4) + P_2^2(P_1^4 + P_3^4) + P_3^2(P_2^4 + P_3^4)) + \\ &a_{123}(P_1^2 P_2^2 P_3^2) + \frac{1}{2S_{11}}(Q_{11}P_1^2 + Q_{12}(P_2^2 + P_3^2) - \varepsilon_{11})^2, \end{aligned} \quad (\text{G5})$$

which simplifies to

$$\begin{aligned} \tilde{f}(T, P_i, \varepsilon_{11}, \sigma_{ij(ij \neq 11)} = 0) &= a_1(P_1^2 + P_2^2 + P_3^2) + a_{11}(P_1^4 + P_2^4 + P_3^4) + a_{12}(P_1^2 P_2^2 + P_2^2 P_3^2 + P_1^2 P_3^2) \\ &+ a_{111}(P_1^6 + P_2^6 + P_3^6) + a_{112}(P_1^2(P_2^4 + P_3^4) + P_2^2(P_1^4 + P_3^4) + P_3^2(P_2^4 + P_3^4)) + \\ &a_{123}(P_1^2 P_2^2 P_3^2) + \frac{1}{2S_{11}}(\varepsilon_{11}^0 - \varepsilon_{11})^2. \end{aligned} \quad (\text{G6})$$

To compute the  $T$ - $\varepsilon_{11}$  stability diagram, we minimize the modified Helmholtz free energy with respect to polarization over the range of possible temperature ( $T$ ) and strain ( $\varepsilon_{11}$ ) conditions to find the homogenous modified Helmholtz free energy of the system. Next, from the thermodynamic theory of strain phase separation [80], we assume that the interfaces between different ferroelectric phases are incoherent, and they possess a negligible interfacial energy. Therefore, we may define the total modified Helmholtz Free Energy density as

$$\tilde{f}^{mix} = \omega^\alpha \tilde{f}^\alpha + \omega^\beta \tilde{f}^\beta, \quad (\text{G7})$$

where thermodynamic equilibrium is achieved when  $\tilde{f}^{mix}$  is minimized subject to the mechanical constraints that require,

$$\varepsilon_{11} = \omega^\alpha \varepsilon_{11}^\alpha + \omega^\beta \varepsilon_{11}^\beta, \quad (\text{G8})$$

and the requirement that the total volume fraction must equal one,  $\omega^\alpha + \omega^\beta = 1$ , which may be found using the common tangent construction approach.

In ferroelectric systems, multiple ferroelectric phases can coexist with identical free-energy profiles as a function of strain, allowing for the existence of more ferroelectric variants, than one may initially expect from Gibbs phase rule. For example, for a tetragonal domain there are six possible ferroelectric variants,  $(\pm P_1, 0, 0)$ ,  $(0, \pm P_2, 0)$  and  $(0, 0, \pm P_3)$ , which can be referred to as  $\pm T_1$ ,  $\pm T_2$ , and  $\pm T_3$ . Under a uniaxial strain, these six possible variants possess, only two unique energy surfaces: one for the  $\pm a_1$  and one for the  $\pm a_2$ , and  $\pm a_3$ , i.e.,

$$f^\alpha(\varepsilon_{11}) = f^{+T_1}(\varepsilon_{11}) = f^{-T_1}(\varepsilon_{11}), \quad (\text{G9a})$$

$$f^\beta(\varepsilon_{11}) = f^{+T_2}(\varepsilon_{11}) = f^{-T_2}(\varepsilon_{11}) = f^{+T_3}(\varepsilon_{11}) = f^{-T_3}(\varepsilon_{11}), \quad (\text{G9b})$$

Consequently, the common tangent construction can calculate the volume fraction of each distinct branch (i.e,  $\alpha$  and  $\beta$ ), but not the individual volume fractions of each degenerate variant within a given branch.

## References

- [1] D. Lu, D. J. Baek, S. S. Hong, L. F. Kourkoutis, Y. Hikita, H. Y. Hwang, Synthesis of freestanding single-crystal perovskite films and heterostructures by etching of sacrificial water-soluble layers, *Nat Mater* 15 (12) (2016) 1255, <https://doi.org/10.1038/nmat4749>.
- [2] H. S. Kum, H. Lee, S. Kim, S. Lindemann, W. Kong, K. Qiao, P. Chen, J. Irwin, J. H. Lee, S. E. Xie, S. Subramanian, J. Shim, S. H. Bae, C. Choi, L. Ranno, S. Seo, S. Lee, J. Bauer, H. S. Li, K. Lee, J. A. Robinson, C. A. Ross, D. G. Schlom, M. S. Rzchowski, C. B. Eom, J. Kim, Heterogeneous integration of single-crystalline complex-oxide membranes, *Nature* 578 (7793) (2020) 75, <https://doi.org/10.1038/s41586-020-1939-z>.
- [3] D. Pesquera, E. Khestanova, M. Ghidini, S. Zhang, A. P. Rooney, F. Maccherozzi, P. Riego, S. Farokhipoor, J. Kim, X. Moya, M. E. Vickers, N. A. Stelmashenko, S. J. Haigh, S. S. Dhesi, N. D. Mathur, Large magnetoelectric coupling in multiferroic oxide heterostructures assembled via epitaxial lift-off, *Nat Commun* 11 (1) (2020) 3190, <https://doi.org/10.1038/s41467-020-16942-x>.
- [4] D. Pesquera, E. Parsonnet, A. Qualls, R. J. Xu, A. J. Gubser, J. Kim, Y. Z. Jiang, G. Velarde, Y. L. Huang, H. Y. Hwang, R. Ramesh, L. W. Martin, Beyond substrates: Strain engineering of ferroelectric membranes, *Adv Mater* 32 (43) (2020) 2003780, <https://doi.org/10.1002/adma.202003780>.
- [5] L. Han, C. Addiego, S. Prokhorenko, M. Y. Wang, H. Y. Fu, Y. Nahas, X. X. Yan, S. H. Cai, T. Q. Wei, Y. H. Fang, H. Z. Liu, D. X. Ji, W. Guo, Z. B. Gu, Y. R. Yang, P. Wang, L. Bellaiche, Y. F. Chen, D. Wu, Y. F. Nie, X. Q. Pan, High-density switchable skyrmion-like polar nanodomains integrated on silicon, *Nature* 603 (7899) (2022) 63, <https://doi.org/10.1038/s41586-021-04338-w>.
- [6] S. Lindemann, J. Irwin, G. Y. Kim, B. Wang, K. Eom, J. J. Wang, J. M. Hu, L. Q. Chen, S. Y. Choi, C. B. Eom, M. S. Rzchowski, Low-voltage magnetoelectric coupling in membrane heterostructures, *Sci Adv* 7 (46) (2021) eabh2294, <https://doi.org/10.1126/sciadv.abh2294>.
- [7] D. X. Du, J. M. Hu, J. K. Kawasaki, Strain and strain gradient engineering in membranes of quantum materials, *Appl Phys Lett* 122 (17) (2023) 170501, <https://doi.org/10.1063/5.0146553>.
- [8] S. S. Hong, M. Q. Gu, M. Verma, V. Harbola, B. Y. Wang, D. Lu, A. Vailionis, Y. Hikita, R. Pentcheva, J. M. Rondinelli, H. Y. Hwang, Extreme tensile strain states in LaCaMnO<sub>3</sub> membranes, *Science* 368 (6486) (2020) 71, <https://doi.org/10.1126/science.aax9753>.
- [9] S. S. Huang, S. Xu, C. Ma, P. Z. Li, E. J. Guo, C. Ge, C. Wang, X. L. Xu, M. He, G. Z. Yang, K. J. Jin, Ferroelectric order evolution in freestanding PbTiO<sub>3</sub> films monitored by optical second harmonic generation, *Adv Sci* 11 (2024) 2307571, <https://doi.org/10.1002/advs.202307571>.
- [10] Y. P. Zang, C. Di, Z. M. Geng, X. J. Yan, D. X. Ji, N. C. Zheng, X. Y. Jiang, H. Y. Fu, J. J. Wang, W. Guo, H. Y. Sun, L. Han, Y. L. Zhou, Z. B. Gu, D. S. Kong, H. Aramberri, C. Cazorla, J. Iñiguez, R. Rurali, L. Q. Chen, J. Zhou, D. Wu, M. H. Lu, Y. F. Nie, Y. F. Chen, X. Q. Pan, Giant thermal transport tuning at a metal/ferroelectric Interface, *Adv Mater* 34 (3) (2022) 2105778, <https://doi.org/10.1002/adma.202105778>.
- [11] G. H. Dong, S. Z. Li, M. T. Yao, Z. Y. Zhou, Y. Q. Zhang, X. Han, Z. L. Luo, J. X. Yao, B.

- Peng, Z. Q. Hu, H. B. Huang, T. T. Jia, J. Y. Li, W. Ren, Z. G. Ye, X. D. Ding, J. Sun, C. W. Nan, L. Q. Chen, J. Li, M. Liu, Super-elastic ferroelectric single-crystal membrane with continuous electric dipole rotation, *Science* 366 (6464) (2019) 475, <https://doi.org/10.1126/science.aay7221>.
- [12] B. Peng, R. C. Peng, Y. Q. Zhang, G. H. Dong, Z. Y. Zhou, Y. Q. Zhou, T. Li, Z. J. Liu, Z. L. Luo, S. H. Wang, Y. Xia, R. B. Qiu, X. X. Cheng, F. Xue, Z. Q. Hu, W. Ren, Z. G. Ye, L. Q. Chen, Z. W. Shan, T. Min, M. Liu, Phase transition enhanced superior elasticity in freestanding single-crystalline multiferroic BiFeO<sub>3</sub> membranes, *Sci Adv* 6 (34) (2020) eaba5847, <https://doi.org/10.1126/sciadv.aba5847>.
- [13] G. H. Dong, S. Z. Li, T. Li, H. J. Wu, T. X. Nan, X. H. Wang, H. X. Liu, Y. X. Cheng, Y. Q. Zhou, W. B. Qu, Y. F. Zhao, B. Peng, Z. G. Wang, Z. Q. Hu, Z. L. Luo, W. Ren, S. J. Pennycook, J. Li, J. Sun, Z. G. Ye, Z. D. Jiang, Z. Y. Zhou, X. D. Ding, T. Min, M. Liu, Periodic wrinkle-patterned single-crystalline ferroelectric oxide membranes with enhanced piezoelectricity, *Adv Mater* 32 (50) (2020) 2004477, <https://doi.org/10.1002/adma.202004477>.
- [14] D. X. Du, S. Manzo, C. Y. Zhang, V. Saraswat, K. T. Genser, K. M. Rabe, P. M. Voyles, M. S. Arnold, J. K. Kawasaki, Epitaxy, exfoliation, and strain-induced magnetism in rippled Heusler membranes, *Nat Commun* 12 (1) (2021) 2494, <https://doi.org/10.1038/s41467-021-22784-y>.
- [15] H. Elangovan, M. Barzilay, S. Seremi, N. Cohen, Y. Z. Jiang, L. W. Martin, Y. Ivry, Giant superelastic piezoelectricity in flexible ferroelectric BaTiO<sub>3</sub> membranes, *Acs Nano* 14 (4) (2020) 5053, <https://doi.org/10.1021/acsnano.0c01615>.
- [16] G. Sánchez-Santolino, V. Rouco, S. Puebla, H. Aramberri, V. Zamora, M. Cabero, F. A. Cuellar, C. Munuera, F. Mompean, M. Garcia-Hernandez, A. Castellanos-Gomez, J. Iñiguez, C. Leon, J. Santamaria, A 2D ferroelectric vortex pattern in twisted BaTiO<sub>3</sub> freestanding layers, *Nature* 626 (7999) (2024) 529, <https://doi.org/10.1038/s41586-023-06978-6>.
- [17] D. G. Schlom, L. Q. Chen, C. J. Fennie, V. Gopalan, D. A. Muller, X. Q. Pan, R. Ramesh, R. Uecker, Elastic strain engineering of ferroic oxides, *MRS Bull* 39 (2) (2014) 118, <https://doi.org/10.1557/mrs.2014.1>.
- [18] S. R. Bakaul, S. Prokhorenko, Q. Zhang, Y. Nahas, Y. S. Hu, A. Petford-Long, L. Bellaiche, N. Valanoor, Freestanding ferroelectric bubble domains, *Adv Mater* 33 (45) (2021) 2105432, <https://doi.org/10.1002/adma.202105432>.
- [19] R. J. Xu, J. W. Huang, E. S. Barnard, S. S. Hong, P. Singh, E. K. Wong, T. Jansen, V. Harbola, J. Xiao, B. Y. Wang, S. Crossley, D. Lu, S. Liu, H. Y. Hwang, Strain-induced room-temperature ferroelectricity in SrTiO<sub>3</sub> membranes, *Nat Commun* 11 (1) (2020) 3141, <https://doi.org/10.1038/s41467-020-16912-3>.
- [20] R. J. Xu, K. J. Crust, V. Harbola, R. Arras, K. Y. Patel, S. Prosandeev, H. Cao, Y. T. Shao, P. Behera, L. Caretta, W. J. Kim, A. Khandelwal, M. Acharya, M. M. Wang, Y. Liu, E. S. Barnard, A. Raja, L. W. Martin, X. W. Gu, H. Zhou, R. Ramesh, D. A. Muller, L. Bellaiche, H. Y. Hwang, Size-induced ferroelectricity in antiferroelectric oxide membranes, *Adv Mater* 35 (17) (2023) 2210562, <https://doi.org/10.1002/adma.202210562>.

- [21] Y. T. Guo, B. Peng, G. M. Lu, G. H. Dong, G. N. Yang, B. H. Chen, R. B. Qiu, H. X. Liu, B. T. Zhang, Y. F. Yao, Y. N. Zhao, S. Z. Li, X. D. Ding, J. Sun, M. Liu, Remarkable flexibility in freestanding single-crystalline antiferroelectric  $\text{PbZrO}_3$  membranes, *Nat Commun* 15 (1) (2024), <https://doi.org/10.1038/s41467-024-47419-w>.
- [22] M. T. Yao, Y. X. Cheng, Z. Y. Zhou, M. Liu, Recent progress on the fabrication and applications of flexible ferroelectric devices, *J Mater Chem C* 8 (1) (2020) 14, <https://doi.org/10.1039/c9tc04706a>.
- [23] P. Muralt, Ferroelectric thin films for micro-sensors and actuators: a review, *J Micromech Microeng* 10 (2) (2000) 136, <https://doi.org/10.1088/0960-1317/10/2/307>.
- [24] S. H. Shin, Y. H. Kim, M. H. Lee, J. Y. Jung, J. Nah, Hemispherically aggregated  $\text{BaTiO}_3$  nanoparticle composite thin film for high-performance flexible piezoelectric nanogenerator, *Acs Nano* 8 (3) (2014) 2766, <https://doi.org/10.1021/nn406481k>.
- [25] G. Z. Zhang, P. Zhao, X. S. Zhang, K. Han, T. K. Zhao, Y. Zhang, C. K. Jeong, S. L. Jiang, S. L. Zhang, Q. Wang, Flexible three-dimensional interconnected piezoelectric ceramic foam based composites for highly efficient concurrent mechanical and thermal energy harvesting, *Energ Environ Sci* 11 (8) (2018) 2046, <https://doi.org/10.1039/c8ee00595h>.
- [26] W. X. Gao, Y. Zhu, Y. J. Wang, G. L. Yuan, J. M. Liu, A review of flexible perovskite oxide ferroelectric films and their application, *J Materiomics* 6 (1) (2020) 1, <https://doi.org/10.1016/j.jmat.2019.11.001>.
- [27] S. Ganguly, D. Pesquera, D. M. Garcia, U. Saeed, N. Mirzamohammadi, J. Santiso, J. Padilla, J. M. C. Roque, C. Laulhé, F. Berenguer, L. G. Villanueva, G. Catalan, Photostrictive actuators based on freestanding ferroelectric membranes, *Adv Mater* 36 (2024) 2310198, <https://doi.org/10.1002/adma.202310198>.
- [28] Q. Li, V. A. Stoica, M. Pasciak, Y. Zhu, Y. K. Yuan, T. N. Yang, M. R. McCarter, S. Das, A. K. Yadav, S. Park, C. Dai, H. J. Lee, Y. Ahn, S. D. Marks, S. K. Yu, C. Kadlec, T. Sato, M. C. Hoffmann, M. Chollet, M. E. Kozina, S. Nelson, D. L. Zhu, D. A. Walko, A. M. Lindenberg, P. G. Evans, L. Q. Chen, R. Ramesh, L. W. Martin, V. Gopalan, J. W. Freeland, J. Hlinka, H. D. Wen, Subterahertz collective dynamics of polar vortices, *Nature* 592 (7854) (2021) 376, <https://doi.org/10.1038/s41586-021-03342-4>.
- [29] T. N. Yang, C. Dai, Q. Li, H. D. Wen, L. Q. Chen, Condensation of collective polar vortex modes, *Phys Rev B* 103, L220303 (2021), <https://doi.org/10.1103/PhysRevB.103.L220303>.
- [30] V. A. Stoica, T. N. Yang, S. Das, Y. Cao, H. Y. Wang, Y. Kubota, C. Dai, H. Padma, Y. Sato, A. Mangu, Q. L. Nguyen, Z. Zhang, D. Talreja, M. E. Zajac, D. A. Walko, A. D. DiChiara, S. Owada, K. Miyanishi, K. Tamasaku, T. Sato, J. M. Glowina, V. Esposito, S. Nelson, M. C. Hoffmann, R. D. Schaller, A. M. Lindenberg, L. W. Martin, R. Ramesh, I. Matsuda, D. L. Zhu, L. Q. Chen, H. D. Wen, V. Gopalan, J. W. Freeland, Non-equilibrium pathways to emergent polar supertextures, *Nat Mater* 23, 1759 (2024), <https://doi.org/10.1038/s41563-024-02044-2>.
- [31] W. Li, S. X. Wang, P. Peng, H. J. Han, X. B. Wang, J. Ma, J. L. Luo, J. M. Liu, J. F. Li, C. W. Nan, Q. Li, Terahertz excitation of collective dynamics of polar skyrmions over a broad temperature range, *Nat Phys* (2025), <https://doi.org/10.1038/s41567-025-03056-8>.
- [32] S. Z. Zheng, J. T. Zhang, A. L. Li, J. Wang, Origin of chiral phase transition of polar vortex

- in ferroelectric/dielectric superlattices, *Nano Lett* 25 (4) (2025) 1397, <https://doi.org/10.1021/acs.nanolett.4c05067>.
- [33] Y. Song, X. M. Shi, J. Wang, H. B. Huang, Ultrafast phase-field model of frequency-dependent dielectric behavior in ferroelectrics, *J Am Ceram Soc* 107 (4) (2024) 2433, <https://doi.org/10.1111/jace.19575>.
- [34] S. Z. Zheng, C. Liu, Y. Zhang, S. B. Shi, T. Xu, T. Shimada, J. Wang, Giant shear-vertical wave bandgaps induced by diffuse domain-walls in ferroelectrics, *Int J Mech Sci* 294 (2025) 110239, <https://doi.org/10.1016/j.ijmecsci.2025.110239>.
- [35] T. N. Yang, B. Wang, J. M. Hu, L. Q. Chen, Domain dynamics under ultrafast electric-field pulses, *Phys Rev Lett* 124 (10) (2020) 107601, <https://doi.org/10.1103/PhysRevLett.124.107601>.
- [36] S. Z. Zheng, X. Hou, P. Han, T. Xu, T. Shimada, J. Wang, Tunable lamb wave bandgap based on 90° diffuse domain walls in ferroelectric thin films, *Acta Mater* 296 (2025) 121284, <https://doi.org/10.1016/j.actamat.2025.121284>.
- [37] H. H. Wang, V. A. Stoica, C. Dai, M. Pasciak, S. Das, T. N. Yang, M. A. P. Gonçalves, J. Kulda, M. R. McCarter, A. Mangu, Y. Cao, H. Padma, U. Saha, D. L. Zhu, T. Sato, S. H. Song, M. C. Hoffmann, P. Kramer, S. Nelson, Y. W. Sun, Q. Nguyen, Z. Zhang, R. Ramesh, L. W. Martin, A. M. Lindenberg, L. Q. Chen, J. W. Freeland, J. Hlinka, V. Gopalan, H. D. Wen, Terahertz-field activation of polar skyrons, *Nat Commun* 16 (1) (2025) 8994, <https://doi.org/10.1038/s41467-025-64033-6>.
- [38] S. H. Zhuang, J. M. Hu, Role of polarization-photon coupling in ultrafast terahertz excitation of ferroelectrics, *Phys Rev B* 106 (14) (2022) L140302, <https://doi.org/10.1103/PhysRevB.106.L140302>.
- [39] Y. J. Zhu, A. Ross, X. W. Guo, V. Gopalan, L. Q. Chen, J. M. Hu, Theory of terahertz pulse transmission through ferroelectric nanomembranes, *Phys Rev B* 112 (9) (2025) 094312, <https://doi.org/10.1103/7wnn-j6nc>.
- [40] Y. J. Zhu, T. R. Chen, A. Ross, B. Wang, X. W. Guo, V. Gopalan, L. Q. Chen, J. M. Hu, Theory of nonlinear terahertz susceptibility in ferroelectrics, *Phys Rev B* 110 (5) (2024) 054311, <https://doi.org/10.1103/PhysRevB.110.054311>.
- [41] T. R. Chen, B. Wang, Y. J. Zhu, S. H. Zhuang, L. Q. Chen, J. M. Hu, Analytical model and dynamical phase-field simulation of terahertz transmission across ferroelectrics, *Phys Rev B* 109 (9) (2024) 094305, <https://doi.org/10.1103/PhysRevB.109.094305>.
- [42] F. Gómez-Ortiz, L. Bastogne, X. He, P. Ghosez, Precise control and displacement of polar textures from inhomogeneous and time-dependent electric fields, *Phys Rev B* 111 (13) (2025) 134107, <https://doi.org/10.1103/PhysRevB.111.134107>.
- [43] L. Bastogne, F. Gómez-Ortiz, S. Anand, P. Ghosez, Dynamical manipulation of polar topologies from acoustic phonon excitations, *Nano Lett* 24 (43) (2024) 13783, <https://doi.org/10.1021/acs.nanolett.4c04125>.
- [44] P. Chen, C. Paillard, H. J. Zhao, J. Iñiguez, L. Bellaiche, Deterministic control of ferroelectric polarization by ultrafast laser pulses, *Nat Commun* 13 (1) (2022) 2566, <https://doi.org/10.1038/s41467-022-30324-5>.

- [45] D. W. Wang, J. Weerasinghe, L. Bellaiche, J. Hlinka, Dynamical coupling in Pb(Zr,Ti)O<sub>3</sub> solid solutions from first principles, *Phys Rev B* 83 (2) (2011) 020301, <https://doi.org/10.1103/PhysRevB.83.020301>.
- [46] M. A. Makeev, S. Rijal, Y. Nahas, S. Prokhorenko, L. Bellaiche, Formation mechanism of quasiordered superstructures of electric bubbles, *Phys Rev B* 111 (6) (2025) L060305, <https://doi.org/10.1103/PhysRevB.111.L060305>.
- [47] S. Rijal, Y. Nahas, S. Prokhorenko, L. Bellaiche, Dynamics of polar vortex crystallization, *Phys Rev Lett* 133 (9) (2024) 096801, <https://doi.org/10.1103/PhysRevLett.133.096801>.
- [48] L. Y. Gao, S. Prokhorenko, Y. Nahas, L. Bellaiche, Dynamical control of topology in polar skyrmions via twisted light, *Phys Rev Lett* 132 (2) (2024) 026902, <https://doi.org/10.1103/PhysRevLett.132.026902>.
- [49] M. A. Makeev, S. Rijal, S. Prokhorenko, Y. Nahas, L. Bellaiche, Quasihexagonal arrays of electric-skyrmion bubbles in thin-film ferroelectrics: Pattern formation and structure, *Phys Rev B* 110 (14) (2024) 144113, <https://doi.org/10.1103/PhysRevB.110.144113>.
- [50] Q. T. Zhang, R. Herchig, I. Ponomareva, Nanodynamics of ferroelectric ultrathin films, *Phys Rev Lett* 107 (17) (2011) 177601, <https://doi.org/10.1103/PhysRevLett.107.177601>.
- [51] J. Y. Yang, S. Liu, Topological phase transitions in perovskite superlattices driven by temperature, electric field, and doping, *Phys Rev B* 110 (21) (2024) 214112, <https://doi.org/10.1103/PhysRevB.110.214112>.
- [52] F. Gómez-Ortiz, M. Graf, J. Junquera, J. Iñiguez-Gonzalez, H. Aramberri, Liquid-crystal-like dynamic transition in ferroelectric-dielectric superlattices, *Phys Rev Lett* 133 (6) (2024) 066801, <https://doi.org/10.1103/PhysRevLett.133.066801>.
- [53] G. Z. Chen, J. Lan, T. Min, J. Xiao, Narrow waveguide based on ferroelectric domain wall, *Chinese Phys Lett* 38 (8) (2021) 087701, <https://doi.org/10.1088/0256-307x/38/8/087701>.
- [54] X. H. Zhou, C. Y. Cai, P. Tang, R. L. Rodríguez-Suárez, S. M. Rezende, G. E. W. Bauer, T. Yu, Surface ferron excitations in ferroelectrics and their directional routing, *Chinese Phys Lett* 40 (8) (2023) 087103, <https://doi.org/10.1088/0256-307x/40/8/087103>.
- [55] R. Khomeriki, K. Dörr, J. Berakdar, Conductive domain walls in ferroelectrics as tunable coherent THz radiation source, arXiv:2509.01542 (2025).
- [56] X. Q. Ke, D. Wang, X. B. Ren, Y. Z. Wang, Polarization spinodal at ferroelectric morphotropic phase boundary, *Phys Rev Lett* 125 (12) (2020) 127602, <https://doi.org/10.1103/PhysRevLett.125.127602>.
- [57] W. Zhong, D. Vanderbilt, K. M. Rabe, Phase-transitions in BaTiO<sub>3</sub> from first principles, *Phys Rev Lett* 73 (13) (1994) 1861, <https://doi.org/10.1103/PhysRevLett.73.1861>.
- [58] P. Chen, L. Ponet, K. J. Lai, R. Cingolani, S. Artyukhin, Domain wall-localized phonons in BiFeO<sub>3</sub>: spectrum and selection rules, *Npj Comput Mater* 6 (1) (2020) 48, <https://doi.org/10.1038/s41524-020-0304-y>.
- [59] S. H. Zhuang, J. M. Hu, Acoustic attenuation in magnetic insulator films: effects of magnon polaron formation, *J Phys D Appl Phys* 56 (5) (2023) 054004, <https://doi.org/10.1088/1361-6463/acae30>.

- [60] C. Kittel, Interaction of spin waves and ultrasonic waves in ferromagnetic crystals, *Phys Rev* 110 (4) (1958) 836, <https://doi.org/10.1103/PhysRev.110.836>.
- [61] S. H. Zhuang, X. F. Zhang, Y. J. Zhu, N. X. Sun, C. B. Eom, P. G. Evans, J. M. Hu, Hybrid magnon-phonon cavity for large-amplitude terahertz spin-wave excitation, *Phys Rev Appl* 21 (4) (2024) 044009, <https://doi.org/10.1103/PhysRevApplied.21.044009>.
- [62] I. Luk'yanchuk, A. Sené, V. M. Vinokur, Electrodynamics of ferroelectric films with negative capacitance, *Phys Rev B* 98 (2) (2018) 024107, <https://doi.org/10.1103/PhysRevB.98.024107>.
- [63] C. Chen, L. Xie, X. W. Guo, G. F. Liang, Z. Wang, Y. Chen, M. H. Qin, X. B. Lu, X. S. Gao, G. F. Zhou, Z. J. Hong, J. M. Liu, D. Y. Chen, Emergence of polar vortex-antivortex pair arrays in multiferroic superlattices, *Adv Mater* (2025), <https://doi.org/10.1002/adma.202501894>.
- [64] W. R. Geng, X. W. Guo, Y. L. Zhu, D. S. Ma, Y. L. Tang, Y. J. Wang, Y. J. Wu, Z. J. Hong, X. L. Ma, Observation of multi-order polar radial vortices and their topological transition, *Nat Commun* 16 (1) (2025) 2804, <https://doi.org/10.1038/s41467-025-58008-w>.
- [65] W. R. Geng, Y. L. Zhu, M. X. Zhu, Y. L. Tang, H. J. Zhao, C. H. Lei, Y. J. Wang, J. H. Wang, R. J. Jiang, S. Z. Liu, X. Y. San, Y. P. Feng, M. J. Zou, X. L. Ma, Dipolar wavevector interference induces a polar skyrmion lattice in strained BiFeO<sub>3</sub> films, *Nat Nanotechnol* (2025), <https://doi.org/10.1038/s41565-024-01845-5>.
- [66] Y. Wang, Y. Tang, Y. Zhu, X. Ma, Entangled polarizations in ferroelectrics: A focused review of polar topologies, *Acta Mater* 243 (2023) 118485, <https://doi.org/10.1016/j.actamat.2022.118485>.
- [67] J. Xu, C. C. Zhong, X. J. Zhou, X. Han, D. F. Jin, S. K. Gray, L. Jiang, X. F. Zhang, Coherent pulse echo in hybrid magnonics with multimode phonons, *Phys Rev Appl* 16 (2) (2021) 024009, <https://doi.org/10.1103/PhysRevApplied.16.024009>.
- [68] Y. Li, C. B. Zhao, W. Zhang, A. Hoffmann, V. Novosad, Advances in coherent coupling between magnons and acoustic phonons, *Apl Mater* 9 (6) (2021) 060902, <https://doi.org/10.1063/5.0047054>.
- [69] J. M. Hu, Design of new-concept magnetomechanical devices by phase-field simulations, *Mrs Bull* 49 (6) (2024) 636, <https://doi.org/10.1557/s43577-024-00699-5>.
- [70] K. An, A. N. Litvinenko, R. Kohno, A. A. Fuad, V. V. Naletov, L. Vila, U. Ebels, G. de Loubens, H. Hurdequint, N. Beaulieu, J. Ben Youssef, N. Vukadinovic, G. E. W. Bauer, A. N. Slavin, V. S. Tiberkevich, O. Klein, Coherent long-range transfer of angular momentum between magnon Kittel modes by phonons, *Phys Rev B* 101 (6) (2020) 060407, <https://doi.org/10.1103/PhysRevB.101.060407>.
- [71] Y. Zhu, J. Wu, A. N. Morozovska, E. A. Eliseev, Y. M. Vysochanskii, V. Gopalan, L.-Q. Chen, X. F. Zhang, W. Zhang, J.-M. Hu, Strong coupling between coherent ferrons and cavity acoustic phonons, arXiv:2511.01201 (2025).
- [72] D. D. Awschalom, C. R. Du, R. He, F. J. Heremans, A. Hoffmann, J. Hou, H. Kurebayashi, Y. Li, L. Q. Liu, V. Novosad, J. Sklenar, S. E. Sullivan, D. L. Sun, H. Tang, V. Tyberkevych, C. Trevillian, A. W. Tsen, L. R. Weiss, W. Zhang, X. F. Zhang, L. Y. Zhao, C. W. Zollitsch,

- Quantum engineering with hybrid magnonic systems and materials, *Ieee T Quantum Eng* 2 (2021) 5500836, <https://doi.org/10.1109/Tqe.2021.3057799>.
- [73] B. Cheng, P. L. Kramer, Z. X. Shen, M. C. Hoffmann, Terahertz-driven local dipolar correlation in a quantum paraelectric, *Phys Rev Lett* 130 (12) (2023) 126902, <https://doi.org/10.1103/PhysRevLett.130.126902>.
- [74] L. Q. Chen, Phase-field method of phase transitions/domain structures in ferroelectric thin films: A review, *J Am Ceram Soc* 91 (6) (2008) 1835, <https://doi.org/10.1111/j.1551-2916.2008.02413.x>.
- [75] J. J. Wang, X. Q. Ma, Q. Li, J. Britson, L. Q. Chen, Phase transitions and domain structures of ferroelectric nanoparticles: Phase field model incorporating strong elastic and dielectric inhomogeneity, *Acta Mater* 61 (20) (2013) 7591, <https://doi.org/10.1016/j.actamat.2013.08.055>.
- [76] Y. L. Li, L. Q. Chen, Temperature-strain phase diagram for BaTiO<sub>3</sub> thin films, *Appl Phys Lett* 88 (7) (2006) 072905, <https://doi.org/10.1063/1.2172744>.
- [77] Y. L. Li, L. E. Cross, L. Q. Chen, A phenomenological thermodynamic potential for BaTiO<sub>3</sub> single crystals, *J Appl Phys* 98 (6) (2005) 064101, <https://doi.org/10.1063/1.2042528>.
- [78] S. R. Johnston, Y. L. Yang, Y. T. Cui, E. Y. Ma, T. Kämpfe, L. M. Eng, J. Zhou, Y. F. Chen, M. H. Lu, Z. X. Shen, Measurement of surface acoustic wave resonances in ferroelectric domains by microwave microscopy, *J Appl Phys* 122 (7) (2017) 074101, <https://doi.org/10.1063/1.4997474>.
- [79] S. Tamura, D. C. Hurley, J. P. Wolfe, Acoustic-phonon propagation in superlattices, *Phys Rev B* 38 (2) (1988) 1427, <https://doi.org/10.1103/PhysRevB.38.1427>.
- [80] B. Wang, L. Q. Chen, Theory of strain phase equilibria and diagrams, *Acta Mater* 274 (2024) 120025, <https://doi.org/10.1016/j.actamat.2024.120025>.